Rapid earthquake-tsunami modeling: The multi-event, multi-segment complexity of the 2024 M_W 7.5 Noto Peninsula Earthquake governs tsunami generation

Fabian Kutschera[1], Zhe Jia[1], Bar Oryan[1], Jeremy Wing Ching Wong[1], Wenyuan Fan[1], Alice-Agnes Gabriel[1,2]

[1]Institute of Geophysics and Planetary Physics, Scripps Institution of Oceanography, University of California San Diego, La Jolla, USA
[2]Institute of Geophysics, Ludwig-Maximilians-Universität München, Munich, Germany

Key Points:

- The earthquake ruptures bilaterally, including six subevents and a re-nucleation episode at its hypocenter 20 seconds after its initiation.
- Our complex subevent model aligns with known fault system geometries and is critical in explaining the observed tsunami.
- Our simulation matches tsunami wave amplitude, timing, and polarity of the leading wave, which are crucial for tsunami early warning.

Corresponding author: Fabian Kutschera, fkutschera@ucsd.edu

Abstract

The January 1st, 2024, moment magnitude (M_W) 7.5 Noto Peninsula earthquake ruptured in complex ways, challenging timely analysis of the tsunami generation. We present rapid and accurate tsunami models informed by a 6-subevent centroid moment tensor (CMT) model that we obtain by inverting teleseismic and strong motion data and validation against geodetic observations. We identify two distinct bilateral rupture episodes, including six subevents and a re-nucleation episode at its hypocenter 20 seconds after its initiation, likely aided by fault weakening. We construct a complex uplift model that aligns with known fault system geometries and is critical in modeling the observed tsunami. Our tsunami simulation can explain wave amplitude, timing, and polarity of the leading wave, which are crucial for tsunami early warning. Analyzing a 2000 multi-CMT solution ensemble and comparing to alternative rapid source models, we highlight the importance of incorporating complex source effects for realistic tsunami simulations.

Plain Language Summary

The 2024 moment magnitude 7.5 New Year's Day Noto Peninsula earthquake ruptured a complex, partially offshore fault system and generated a tsunami in the Sea of Japan. We use seismic data to show that the earthquake can be characterized by six distinct subevents, with an initial predominantly onshore rupture propagation towards the southwest and a 20-second delayed second rupture onset towards the northeast, mostly offshore. We use the information we gain from these subevents, such as location and faulting mechanism, to infer the seafloor movement, which informs tsunami simulations. The reconstruction of the earthquake rupture process is not unique. This allows us to explore the influence of source uncertainties on the modeled tsunami, highlighting the importance of complex source effects for tsunami generation. We find that our preferred model matches tsunami onset times, first-motion polarities, and initial wave amplitudes, crucial aspects for tsunami early warning.

1 Introduction

The January 1st, 2024 M_W 7.5 Noto Peninsula (Noto-Hanto) earthquake ruptured an active submarine fault system (Fig. 1, MLIT (2014); Sato et al. (2020)) causing strong ground shaking and a large tsunami within the Sea of Japan. Early analysis points to an unusually complex rupture process, with rapidly estimated slip distributions differing considerably (Fujii & Satake, 2024; Masuda et al., 2024; Okuwaki et al., 2024; U.S. Geological Survey, 2024).

Rapid finite-fault models based on teleseismic data were available within hours after the event (The Headquarters for Earthquake Research Promotion, 2024; U.S. Geological Survey, 2024). The United States Geological Survey (USGS) released a first version obtained solely from the teleseismic data (hereafter model "USGS-T", Fig. S1). Later, the USGS released an updated model using both the teleseismic and Global Navigation Satellite System (GNSS) data (hereafter model "USGS-T+G", Sec. 2.3). This model differs starkly from the earlier version. Specifically, the updated USGS-T+G model does not have a significant offshore slip.

Another finite-fault model is obtained using 53 GNSS stations across the Noto Peninsula, placing the majority of slip onshore or near the northern shoreline of Noto Peninsula (Fujii & Satake, 2024). In contrast to the USGS-T+G model, a finite-fault model from tsunami waveforms recorded around the Sea of Japan places most of the slip offshore (Fujii & Satake, 2024). Additionally, Masuda et al. (2024) investigated landslide contributions to local tsunami generation, but precise reconstruction is challenged by the limited regional bathymetry resolution. Source complexity is important for tsunami generation and propagation (Abrahams et al., 2023; Dettmer et al., 2016; Lotto et al., 2018;

Wirp et al., 2021). Thus, vastly different source models will have different implications for understanding the observed tsunami generation and early warning.

This study aims to address the challenge of rapidly and robustly resolving earthquake rupture complexities and properly translating those complexities to inform accurate tsunami simulations. We present rapid and accurate tsunami simulations constructing complex seafloor displacements from a Bayesian 6-subevent centroid moment tensor (CMT) model that we obtain using teleseismic and strong motion observations of the Noto Peninsula earthquake. We unify seismic and tsunami observations in agreement with geodetic data. While CMT solutions are rapidly available, they are rarely used in routine tsunami modeling or early warning contexts (Gusman & Tanioka, 2014; Miyoshi et al., 2015). To the best of our knowledge, this study is the first to use a multi-CMT model to source a tsunami simulation. We demonstrate that our approach captures key characteristics of the tsunami complexities better than other rapid finite-fault inversion approaches and discuss the effects of source complexity and its uncertainties on tsunami modeling based on an ensemble of 2000 multi-CMT solutions.

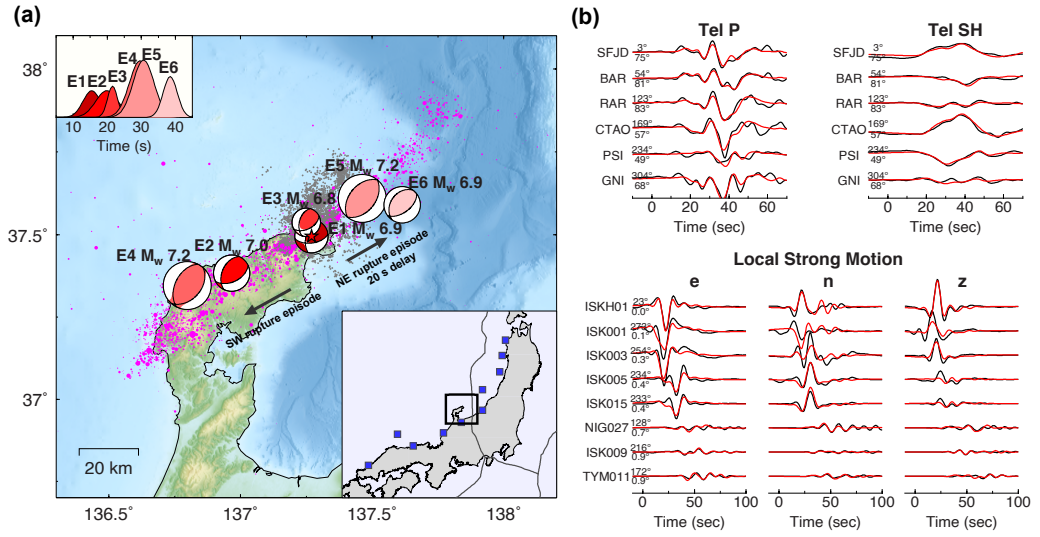

Figure 1. (a) Overview of the Noto Peninsula, Japan, study area. The red star indicates the JMA epicenter of the January 1, 2024, M_W 7.5 Noto Peninsula earthquake. The red focal mechanisms are the six subevents of the Bayesian multi-centroid moment tensor (CMT) inversion using teleseismic and regional strong motion data. The earthquake first initiates towards the southwest, indicated by subevents E1, E2, and E4. After a delay of 20 s, the rupture unfolds towards the northeast, as indicated by subevents E3, E5, and E6. The focal mechanisms are color-coded with respect to time, and the corresponding Gaussian source time durations are shown in the top left figure inset. The blue squares in the bottom right figure inset mark the position of tide gauges facing the Sea of Japan. (b) Comparison of selected observed teleseismic P, SH, and local strong ground motion recordings (black) with the corresponding synthetic seismic waveforms (red) of the preferred multi-CMT solution. The numbers leading the traces are the respective azimuth and distance. A complete comparison of all seismic waveforms is shown in Figs. S2-S7.

2 Methods

2.1 Seismic Multi-Centroid Moment Tensor Inversion

We constrain the event's rupture propagation using a multiple CMT subevent inversion method (Tsai et al., 2005; Minson & Dreger, 2008; Jia et al., 2022, 2023). We iteratively increase the number of subevents to achieve a 65% waveform misfit reduction (Figs. S2-S6). The preferred model includes six subevents, E1 to E6, ordered by their centroid time (Fig. 1). Each subevent is characterized by 10 unknowns: centroid time, duration, longitude, latitude, depth, and the five independent components of the symmetric and zero-traced moment tensor (Fig. S8, Table S1). We fix the longitude and latitude of the first subevent at the JMA (Japan Meteorological Agency) epicenter location while solving for its depth.

We use a Metropolis–Hasting Markov Chain Monte Carlo (MCMC) method to sample the posterior probability density function in a Bayesian framework. This MCMC inversion first searches the centroid time, duration, longitude, latitude, and depth and then linearly solves for the independent moment tensor components (Jia et al., 2020, 2022, 2023). As a prior constraining subevent locations, we use the horizontal spatial density of the first three days of aftershocks. We run the MCMC inversion for 15,000 iterations and consider the first 10,000 samples as the burn-in period. This burn-in process ensures a misfit convergence with fluctuations of less than 10% from the optimal model. The randomness of the initial model can significantly influence the MCMC convergence, with an unfortunate draw potentially trapping a chain in a local minimum (Olalotiti-Lawal & Datta-Gupta, 2018; Ray et al., 2013). Therefore, we remove the least-performing 75% of chains, retaining the best-fitting 48 of all 192 chains to reflect the primary posterior probability features. In total, we obtain an ensemble of 240,000 permissible multi-CMT solutions.

We choose the preferred multi-CMT model based on minimizing the seismic waveform misfit. We use 93 teleseismic P and SH waveforms in an epicentral distance range of 30° to 90° obtained from the EarthScope Data Management Center (DMC; Albuquerque Seismological Laboratory/USGS, 2014). Additionally, we use 53 three-component regional KIK-net and K-net strong ground motion waveforms within an epicentral distance of 150 km from National Research Institute for Earth Science and Disaster Prevention (NIED; Okada et al., 2004). We remove the instrument response and detrend the data. We bandpass filter the teleseismic waveforms between 0.005–0.2 Hz and the strong ground motion data between 0.01–0.1 Hz. During the inversion of regional strong motion data, we adopt the JMA2001 1D velocity model (Ueno, 2002), and use a frequency-wavenumber method (L. Zhu & Rivera, 2002) to calculate the Green's functions. For the inversion of teleseismic waves, we calculate the Green's functions with a hybrid method that combines propagator matrix and ray theory (Kikuchi & Kanamori, 1982; Qian et al., 2017), and use a combination of the JMA2001 model for the crust with an IASPEI91 model (Kennett & Engdahl, 1991) describing the deeper earth.

2.2 Mapping the Subevent Model to Seafloor Deformation

We construct a six-fault-segment slip model based on the preferred subevent model (Table S2), assuming rectangular faults. Each fault segment is located at the respective subevent centroid location. We determine their dip, strike, and rake angles from the preferred multi-CMT solution. E1-E5 are considered southeast dipping, and E6, located in the northeast of Noto Peninsula, dips towards the northwest. Each fault segment has an along-strike length of 25 km and extends from the surface with an along-dip depth twice its centroid depth.

Informed by the preferred multi-CMT model, we assume a uniform slip distribution across each of the six fault segments, which we obtain from each respective subevent's

seismic moment and an assumed rigidity of 35 GPa, which resembles the mean rigidity of the shallowest 25 km as given by the JMA2001 velocity model (Ueno, 2002) and is similar to the assumed value in Fujii and Satake (2024); Masuda et al. (2024). We then use an analytic elastic dislocation model (Okada, 1985, 1992) to obtain the corresponding surface displacements.

To evaluate the uncertainties in surface deformation and its impact on tsunami generation, we repeat this analysis for 2000 randomly selected realizations out of the 240,000 MCMC ensemble solutions (Fig. S9, Table S3). We use the sum of the absolute offshore vertical displacement due to the 2000 multi-CMT solutions as a metric to identify two endmember multi-CMT solutions, the minimum and maximum uplift CMT solutions, which yield the least and the most amount of offshore vertical displacements (Fig. S10), respectively.

2.3 USGS Finite-Fault Models

We compare the surface deformation and resulting tsunami of the multi-CMT solution to two USGS finite-fault models (U.S. Geological Survey, 2024). The USGS publishes finite-fault models for M≥7 earthquakes within a few hours (Thompson et al., 2019). These models are crucial for rapid response management and urgent seismic and tsunami hazard assessment. For the 2024 Noto earthquake, the USGS released an initial version of a finite-fault model (USGS-T), which is obtained from broadband teleseismic P, SH, and long-period surface waves after 2.5 hours (Ji et al., 2002). On 10 January 2024, the USGS released an updated finite-fault model (USGS-T+G), which incorporates additional regional GNSS observations in the inversion (Goldberg et al., 2022). We compute surface deformation due to both USGS finite fault models, following the same Okada approaches for our multi-CMT solution (Sec. 2.2). These models are then used to simulate tsunamis and compared to our preferred model.

2.4 Tsunami Simulations

We use GeoClaw and the vertical offshore surface deformation as instantaneous sources for tsunami simulations. GeoClaw is part of the open-source software package ClawPack (LeVeque et al., 2011; Berger et al., 2011; Mandli et al., 2016), which solves the 2D depth-averaged shallow water equations and has been validated against community benchmark problems and real observations (LeVeque & George, 2008; González et al., 2011; Arcos & LeVeque, 2015). The algorithm has been successfully applied to model the 2004 Sumatra tsunami (Ulrich et al., 2022) and the 2017 Tehuantepec tsunami in Mexico (Melgar & Ruiz-Angulo, 2018).

We utilize space-time adaptive mesh refinement with a maximum level of 3 for all tsunami simulations. This results in a maximum spatial resolution of 493 m. We use gridded bathymetry data (GEBCO Compilation Group, 2023) with a resolution of 15 arc seconds (450 m). We note that without rapidly available high-resolution bathymetry and due to interpolation differences in station locations obtained from the Flanders Marine Institute (VLIZ), Intergovernmental Oceanographic Commission (IOC) (2024) and Geospatial Information Authority of Japan (GSI) (2024), we move the location of all tidal stations besides stations Tobishima and Oga to the nearest "wet" cell (Wang et al., 2020), which has minimal impact on our tsunami results. We define the sea surface height anomaly (ssha) as the deviation from the ocean surface at rest. We simulate all tsunami scenarios for three hours, which requires ∼7.5 h per simulation on a laptop (MacBook Air with Apple M2 processor).

We validate our simulated tsunami waveforms with sea level observations obtained from the IOC and the GSI. First, we use the LOWESS algorithm (Locally Weighted Scatterplot Smoothing; Cleveland, 1979; Romano et al., 2021) to remove first-order tidal trends.

Next, we trim the data to three hours after the mainshock origin time (2024-01-01 7:10:22.5 UTC; provided by the JMA) before applying a 300 s lowpass filter. To quantify the similarity of the simulated and observed first-arriving wave packet at all tide gauges, we calculate the cross-correlation coefficient for a 20 min time window, starting 5 min before the arrival of the peak of the initial tsunami crest (Table S4).

3 Results

3.1 Multi-event, Multi-segment Rupture of the 2024 M_W 7.5 Noto Earthquake

Our subevent model reveals two distinct rupture episodes (Fig. 1). Initially, rupture propagates towards the southwest (subevents E1, E2, and E4), lasting for about 30 seconds. Following a delay of 20 s, while the southwest rupture is ongoing, the rupture re-nucleates around the hypocenter (E3) and propagates bilaterally towards the northeast direction (E5 and E6) for 15 seconds.

The geometry of our preferred six-fault-segment slip model aligns with regional mapped fault traces (Fig. S10; Fujii & Satake, 2024; MLIT, 2014) and spatially coincides with the first 30-hour aftershock sequence (Movie S1). The hypocentral subevents E1 and E3 are collocated with four year swarm activity preceding the Noto earthquake (Hubbard & Bradley, 2024; Nishimura et al., 2023; Yoshida et al., 2023).

These six subevents share similar reverse-faulting focal mechanisms, albeit varying significantly in size and duration. The nucleation and re-nucleation subevents, E1 and E3, have the smallest moment magnitudes (both M_W 6.9). The two largest subevents, E4 and E5, each with M_W 7.2, are located near the two endpoints of rupture. Subevents E2, E4, and E5 each have a source duration of ∼13 s, while the duration for the other three subevents is shorter and ranges between ∼6-11 s.

Robust estimates of event depth and fault geometry are critical for simulating the surface deformation and associated tsunami. Using the ensemble of 240,000 multi-CMT solutions, we analyze source parameter uncertainties. We find that the subevent depths are well-constrained ($\leq$10 km) for all subevents (Fig. S8), with an average standard deviation of 1.17 km. All subevent focal mechanisms, except that of E3, also exhibit low uncertainties in strike, dip and rake, with average standard deviations of 15.9°, 4.9°, and 21.3°, respectively (Fig. S9 and Table S3). The geometry of the renucleation subevent E3 has distinctly larger uncertainties, with 88.9°, 14.7°, and 101.1°, in strike, dip, and rake, which likely arise from its concurrence with ongoing southwest rupture, challenging resolution. However, subevent E3 is necessary to explain the closest strong motion waves (Fig. S7).

3.2 Complex Onshore and Offshore Surface Deformation

The synthetic surface displacements due to the complex rupture of the Noto earthquake show a peak vertical offshore uplift of 3.91 m. Our synthetic surface deformation match the regional GNSS observations, showing a broad uplift across the northern Noto Peninsula and subtle subsidence in the far-field (Fig. 2a). Subevents E1–E4 result in a combination of onshore and offshore surface deformation, while the uplift generated by subevents E5 and E6 is located entirely offshore (Fig. 2). The respective northeast rupture episode releases 40% of the seismic moment, translating into up to 5.27 m of offshore fault slip.

Our model predicts less vertical motion than the one recorded at station J576. However, both the USGS-T+G model and the finite-fault model from Fujii and Satake (2024) cannot fully capture the amount of observed subsidence at this site either (e.g., Fig. S1),

suggesting it may be affected by local processes such as landslides or liquefaction (Gomez, 2024; Kataoka et al., 2024).

Our predicted subevent surface displacement produces substantial vertical motion offshore compared to the limited amount of uplift suggested by USGS-T+G and USGS-T models (Fig. 2). The latter (Fig. S1) predicts an offshore vertical uplift up to 1.38 m (Fig. 2b), while the USGS-T+G model (Fig. 2c) predicts a negligible amount of uplift in the northeast of Noto Peninsula (Fig. S1). These differences directly affect the tsunami simulations (Sec. 3.3).

We evaluate the effects of source parameter uncertainties on predicted surface displacement and the associated tsunami simulations. We examine the surface deformations caused by 2000 permissible multi-CMT solutions. The peak offshore uplift varies considerably and has a standard deviation of 1.43 m (Fig. 4a). The minimum uplift CMT model locates the subevents E1-E4 further landwards and produces a significantly reduced offshore uplift of up to 3.02 m (Fig. S10b). The maximum uplift model locates subevents E1-E4 mostly offshore, leading to a large offshore uplift of up to 4.26 m (Fig. S10c).

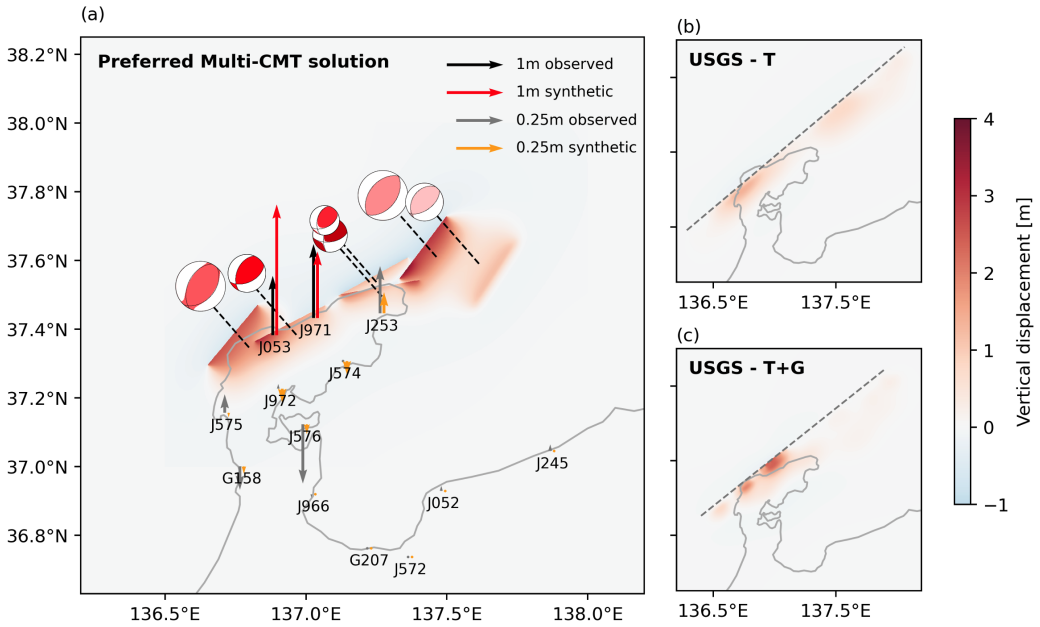

Figure 2. Synthetic vertical displacement constructed from (a) the preferred multi-CMT model, (b) the USGS-T, and (c) the USGS-T+G finite-fault models using an Okada approach. The color-coded vertical arrows show the observed and synthetic vertical displacement at GNSS sites, respectively. The six subevents of the preferred multi-CMT solution are indicated by their moment-tensor solutions. Grey lines in panels (b), (c) represent the fault trace of the respective USGS finite-fault model.

3.3 Complex Tsunami in the Sea of Japan

Our tsunami simulation shows complex coastal wave behavior (Movie S2), including wave crests bending parallel to the coastline due to refraction at the shoaling bathymetry (Fig. 3a). Our simulated tsunami waves capture the timing, initial polarity, and amplitude of the first-arriving crest at all nine tide gauges shown in Fig. 3, and the overall shape of the observed tsunami waveforms at most of them. Specifically, the timing, crucial for tsunami early warning, is captured with high accuracy (within 1 to 3.5 minutes depend-

ing on station distance, Fig. 3b). We achieve overall high cross-correlation coefficients (Sec. 2.4) between the synthetics and observations during the first tsunami wave packet (Fig. 3b). However, it is challenging to fully capture the waveform complexity at the tide gauge Toyama (Fig. S11).

During the three hours of tsunami propagation modeled, our simulated amplitudes agreed with observations within six centimeters at Kashiwazaki, Tajiri, Oga, Saigo, and Okushiri stations. At Sado, Tobishima, and Fukaura stations, the fit of early waves is equally good but the model underestimates the amplitudes of later, trailing signals (Fig. 4b). The maximum tsunami wave amplitude distribution from our preferred simulation (Fig. 4a) indicates a large maximum tsunami height of up to 2.71 m in the source region. Our simulation reveals long-lasting tsunami reverberations around the Noto Peninsula, appearing after 1 hour and 12 minutes (Fig. 3a, Movie S2). Such reverberations may be caused by trapped waves, causing energetic edge waves and/or shelf resonance, as has been observed during the tsunami caused by the M_W 8.2 Tehuantepec, Mexico, earthquake (Melgar & Ruiz-Angulo, 2018).

The tsunami simulation sourced by the minimum-uplift endmember of our source model ensemble underestimates tsunami amplitudes (peak 2.38 m; Fig. 4b, d, Fig. S12, Table S5). In distinction, the tsunami corresponding to the maximum uplift source yields a 24% larger peak tsunami height of up to 3.36 m compared to our preferred tsunami model (Fig. 4b e). Both rapidly available USGS source models generate localized tsunami (Fig. 4b, f, g), but neither can explain the observed tsunami amplitudes and timing (Fig. S13).

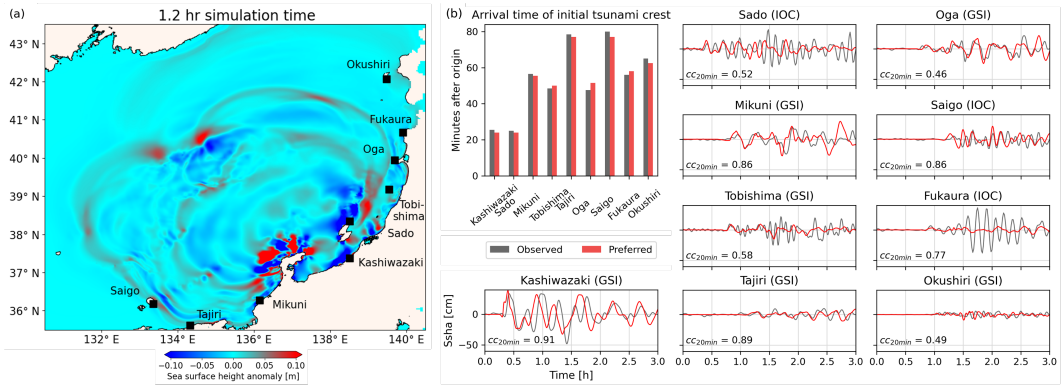

Figure 3. (a) Snapshot of tsunami propagation after 1 hour and 12 minutes simulated time, with strong tsunami reverberations surrounding the Noto Peninsula. At this point in time, towards the northeast, the tsunami reached the tide gauges Oga and Tobishima. In the southwest, the tsunami front arrives at tide gauges Saigo and Tajiri. (b) Comparison of observed and simulated tsunami arrival times and comparison of tsunami waveforms at nine tide gauges. Stations are ordered by their geodetic distance from subevent E1 (Fig. 1).

4 Discussion

An active seismic swarm preceded the M_W 7.5 Noto earthquake (Nishimura et al., 2023), recorded by a dense regional seismic network including events down to magnitude -3 (Hubbard & Bradley, 2024; Japan Meteorological Agency, 2024). Dominated by earthquakes at depths of 14-16 km this swarm led to over 70 mm of surface uplift (Nishimura et al., 2023). Since November 2020, the swarm's activity has fluctuated, including a period of quiescence followed by a M_W 6.2 earthquake in May 2023, the largest event prior to the 2024 Noto earthquake (Kato & Nishimura, 2024). During the two weeks leading

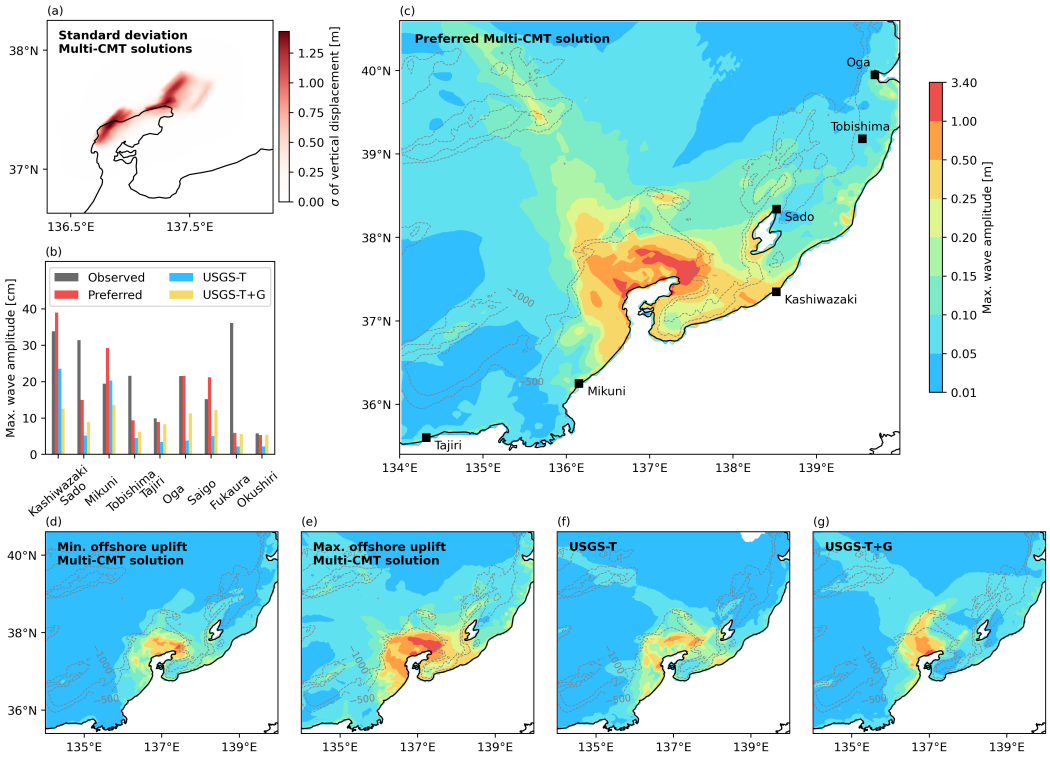

Figure 4. (a) Standard deviation of the vertical displacements based on an ensemble of 2000 multi-CMT solutions. (b) Histogram of the observed and simulated maximum wave amplitudes over a three-hour time window after the earthquake's origin time at the tide gauge locations shown in Fig. 3a. (c) Tsunami maximum wave amplitude distribution sourced by the preferred multi-CMT solution. (d), (e) Tsunami maximum wave amplitude distributions based on the minimum and maximum uplift multi-CMT solutions, respectively. (f), (g) Tsunami maximum wave amplitude distributions modeled using the USGS-T and USGS-T+G source models, respectively.

up to the main shock, a foreshock sequence developed, localizing within a 1 km radius of what would form the Noto earthquake's hypocenter within one hour before its origin time (Kato & Nishimura, 2024).

The spatial and temporal correlation between the swarm activity and the Noto earthquake may suggest a causal relationship with the event's complexity (Okuwaki et al., 2024; Yoshida et al., 2023). Our results indicate that the hypocentral region slipped more than once during the same earthquake, an effect that has been observed in laboratory experiments (Nielsen et al., 2010) and during other large earthquakes (Lee et al., 2006; Wald et al., 1990), including the 2011 Tohoku-Oki event (Lee et al., 2011; Yao et al., 2011) and that has been explained by weakened faults in theoretical and numerical analysis (Gabriel et al., 2012; Nielsen & Madariaga, 2003).

Earthquake swarms have been linked to aseismic slip or fluid migration (Lohman & McGuire, 2007; Ross et al., 2020). Related cyclic changes in pressure, permeability and fluid migration have been observed in a wide range of fault settings (e.g., Gosselin et al., 2020; Ross et al., 2020; Zal et al., 2020). Here, upward fluid migration due to fault valving (Sibson, 1992; W. Zhu et al., 2020) may have aided not only the nucleation but also the rupture and tsunami complexity of the 2024 Noto events. The permeability of

the Noto fault system could have been low during its late interseismic period, allowing high pore-fluid pressure to effectively weaken the fault (Madden et al., 2022; Rice, 1992).

Well recorded moderate and large earthquakes have been shown to rupture complex fault networks in a variety of tectonic settings, involving subevents with distinct fault geometries (Hamling et al., 2017; Jia et al., 2023; Taufiqurrahman et al., 2023; Xu et al., 2023). We find that the Noto earthquake included six subevents rupturing multiple fault segments with different configurations: while the first five subevents likely break faults dipping towards the southeast direction, subevent E6 occurs on a northwest-dipping fault. Such complexity may reflect the complicated regional tectonic setting transitioning between right-lateral strike slip faults and thrust faults in proximity to the Toyama Trough (Ishiyama et al., 2017; Oike & Huzita, 1988). It also agrees with a two-segment finite-fault model, which include information on fault orientations (Okuwaki et al., 2024).

Our subevent model demonstrates that resolving the moment release and associated fault location and geometry is critical to inform tsunami rapid response efforts. Our tsunami simulation can explain the initial tsunami wave packets at most stations. However, local discrepancies remain, including underestimating the observed tsunami heights at stations Fukaura (Fig. 3) and Toyama Bay (Fig. S11), which are likely due to (i) limited resolution of bathymetry; and/or (ii) unmodeled effects of landslides. Bathymetry uncertainties are expected to have less impact on leading waves and their arrival times than on the trailing waves (Sepúlveda et al., 2020). Extensive landsliding has been reported shortly after the Noto Peninsula earthquake (Gomez, 2024; Matsushi, 2024), which may have locally affected the tsunami within Toyama Bay (Fujii & Satake, 2024; Koshimura et al., 2024; Masuda et al., 2024).

5 Conclusions

In this study, we unravel the complex rupture dynamics of the 2024 M_W 7.5 Noto Peninsula earthquake using a 6-subevent centroid moment tensor model that we obtain from teleseismic and strong motion Bayesian inversion. We observe two distinct rupture episodes: an initial, onshore rupture towards the southwest followed by a subsequent, partly offshore rupture towards the northeast, which re-nucleates at the earthquake's hypocenter after a 20-second delay and causes significant seafloor uplift releasing 40% of the total seismic moment. Using the complex subevent model to simulate the resultant coastal tsunami yields large tsunami waves of up to 2.71 m in the source region. Our simulation accurately captures tsunami first arrival timing and overall wave amplitudes. Upon comparison with alternative source models, our findings imply the necessity of using accurate earthquake models that incorporate realistic fault geometries for rapid tsunami modeling and early warning.

Open Research

The original tide gauge data are obtained from the Intergovernmental Oceanographic Commission (IOC; `http://www.ioc-sealevelmonitoring.org`; last access: 1 April 2024) and from the Geospatial Information Authority of Japan (GSI; `https://www.gsi.go.jp/kanshi/tide_furnish.html`; last access: 1 April 2024). GeoClaw has been used for tsunami modeling (Clawpack Development Team, 2023). Our teleseismic data are from EarthScope (formerly IRIS) DMC (Albuquerque Seismological Laboratory/USGS, 2014). Regional strong motion data comes from the NIED strong-motion seismograph networks K-net and KIK-net (Okada et al., 2004). Statsmodels (Seabold & Perktold, 2010) and ObsPy (Beyreuther et al., 2010; Krischer et al., 2015) were used for data processsing, Matplotlib (Hunter, 2007) and the Generic Mapping Tools (Wessel, 2024) for plotting. The geodetic data are obtained from Nevada Geodetic Laboratory (`http://geodesy.unr.edu`, last access: 1 April 2024) and GEONET, which is operated by the GSI.

Acknowledgments

We thank Ryo Okuwaki, Ignacio Sepúlveda, Jorge Macías Sánchez, and Thomas Ulrich for fruitful discussions. We thank the IOC and the GSI for making the sea level recordings at the tide gauges in the Sea of Japan freely available. The authors acknowledge funding from from the National Science Foundation (grant nos. EAR-2225286, EAR-2121568, OAC-2139536, OAC-2311208, NSF EAR-2022441, EAR-2143413), from the European Union's Horizon 2020 research and innovation programme (TEAR ERC Starting; grant no. 852992) and Horizon Europe (ChEESE-2P, grant no. 101093038; DT-GEO, grant no. 101058129; and Geo-INQUIRE, grant no. 101058518), the National Aeronautics and Space Administration (grant no. 80NSSC20K0495) and the Green's Foundation at IGPP at SIO.

References

Abrahams, L. S., Krenz, L., Dunham, E. M., Gabriel, A.-A., & Saito, T. (2023). Comparison of methods for coupled earthquake and tsunami modelling. *Geophysical Journal International*, *234*(1), 404–426. doi: 10.1093/GJI/GGAD053

Albuquerque Seismological Laboratory/USGS. (2014). *Global seismograph network (GSN - IRIS/USGS).* International Federation of Digital Seismograph Networks. doi: 10.7914/SN/IU

Arcos, M. E., & LeVeque, R. J. (2015). Validating Velocities in the GeoClaw Tsunami Model Using Observations near Hawaii from the 2011 Tohoku Tsunami. *Pure and Applied Geophysics*, *172*(3-4), 849–867. doi: 10.1007/S00024-014-0980-Y

Berger, M. J., George, D. L., LeVeque, R. J., & Mandli, K. T. (2011). The GeoClaw software for depth-averaged flows with adaptive refinement. *Advances in Water Resources*, *34*(9), 1195–1206. doi: 10.1016/j.advwatres.2011.02.016

Beyreuther, M., Barsch, R., Krischer, L., Megies, T., Behr, Y., & Wassermann, J. (2010). ObsPy: A Python Toolbox for Seismology. *Seismological Research Letters*, *81*(3), 530–533. doi: 10.1785/gssrl.81.3.530

Clawpack Development Team. (2023). *Clawpack v5.9.2.* Zenodo. doi: 10.5281/zenodo.10076317

Cleveland, W. S. (1979). Robust Locally Weighted Regression and Smoothing Scatterplots. *Journal of the American Statistical Association*, *74*(368), 829–836.

Dettmer, J., Hawkins, R., Cummins, P. R., Hossen, J., Sambridge, M., Hino, R., & Inazu, D. (2016). Tsunami source uncertainty estimation: The 2011 Japan tsunami. *Journal of Geophysical Research: Solid Earth*, *121*(6), 4483–4505. doi: 10.1002/2015JB012764

Flanders Marine Institute (VLIZ), Intergovernmental Oceanographic Commission (IOC). (2024). *Sea level station monitoring facility.* Retrieved from `https://www.ioc-sealevelmonitoring.org` doi: 10.14284/482

Fujii, Y., & Satake, K. (2024). Slip distribution of the 2024 Noto Peninsula earthquake (MJMA 7.6) estimated from tsunami waveforms and GNSS data. *Earth, Planets and Space*, *76*(1), 44. doi: 10.1186/s40623-024-01991-z

Gabriel, A.-A., Ampuero, J.-P., Dalguer, L. A., & Mai, P. M. (2012). The transition of dynamic rupture styles in elastic media under velocity-weakening friction. *Journal of Geophysical Research: Solid Earth*, *117*(B9). doi: 10.1029/2012JB009468

GEBCO Compilation Group. (2023). *GEBCO 2023 Grid.* doi: 10.5285/f98b053b-0cbc-6c23-e053-6c86abc0af7b

Geospatial Information Authority of Japan (GSI). (2024). *Tide level data provided by Geospatial Information Authority of Japan List of tidal stations (in Japanese).* Retrieved from `https://www.gsi.go.jp/kanshi/tide_furnish.html`

Goldberg, D. E., Koch, P., Melgar, D., Riquelme, S., & Yeck, W. L. (2022). Be-

yond the Teleseism: Introducing Regional Seismic and Geodetic Data into Routine USGS Finite-Fault Modeling. *Seismological Research Letters*, *93*(6), 3308–3323. doi: 10.1785/0220220047

Gomez, C. (2024). *The January 1 st 2024 Noto Peninsula Co-seismic Landslides Hazards: Preliminary Results* [preprint]. doi: 10.21203/rs.3.rs-3904468/v1

González, F. I., LeVeque, R. J., Chamberlain, P., Hirai, B., Varkovitzky, J., & George, D. L. (2011). Validation of the GeoClaw model. In (pp. 1–84). GeoClaw Tsunami Modeling Group University of Washington.

Gosselin, J. M., Audet, P., Estève, C., McLellan, M., Mosher, S. G., & Schaeffer, A. J. (2020). Seismic evidence for megathrust fault-valve behavior during episodic tremor and slip. *Science Advances*, *6*(4), eaay5174. doi: 10.1126/sciadv.aay5174

Gusman, A. R., & Tanioka, Y. (2014). W Phase Inversion and Tsunami Inundation Modeling for Tsunami Early Warning: Case Study for the 2011 Tohoku Event. *Pure and Applied Geophysics*, *171*(7), 1409–1422. doi: 10.1007/s00024-013-0680-z

Hamling, I. J., Hreinsdóttir, S., Clark, K., Elliott, J., Liang, C., Fielding, E., ... Stirling, M. (2017). Complex multifault rupture during the 2016 Mw 7.8 Kaikōura earthquake, New Zealand. *Science*, *356*(6334), eaam7194. doi: 10.1126/science.aam7194

Hubbard, J. A., & Bradley, K. (2024). Seismicity patterns around the Jan 1 earthquake in Japan. *Earthquake Insights*. doi: 10.62481/72ea1b55

Hunter, J. D. (2007). Matplotlib: A 2D Graphics Environment. *Computing in Science & Engineering*, *9*(3), 90–95. (Conference Name: Computing in Science & Engineering) doi: 10.1109/MCSE.2007.55

Ishiyama, T., Sato, H., Kato, N., Koshiya, S., Abe, S., Shiraishi, K., & Matsubara, M. (2017). Structures and active tectonics of compressionally reactivated back-arc failed rift across the Toyama trough in the Sea of Japan, revealed by multiscale seismic profiling. *Tectonophysics*, *710-711*, 21–36. doi: 10.1016/j.tecto.2016.09.029

Japan Meteorological Agency. (2024). *The Seismological Bulletin of Japan.* Retrieved from `https://www.data.jma.go.jp/svd/eqev/data/bulletin/hypo_e.html`

Ji, C., Wald, D. J., & Helmberger, D. V. (2002). Source Description of the 1999 Hector Mine, California, Earthquake, Part I: Wavelet Domain Inversion Theory and Resolution Analysis. *Bulletin of the Seismological Society of America*, *92*(4), 1192–1207. doi: 10.1785/0120000916

Jia, Z., Jin, Z., Marchandon, M., Ulrich, T., Gabriel, A.-A., Fan, W., ... Fialko, Y. (2023). The complex dynamics of the 2023 Kahramanmaraş, Turkey, Mw 7.8-7.7 earthquake doublet. *Science*, *381*(6661), 985–990. doi: 10.1126/science.adi0685

Jia, Z., Shen, Z., Zhan, Z., Li, C., Peng, Z., & Gurnis, M. (2020). The 2018 Fiji Mw 8.2 and 7.9 deep earthquakes: One doublet in two slabs. *Earth and Planetary Science Letters*, *531*, 115997. doi: 10.1016/j.epsl.2019.115997

Jia, Z., Zhan, Z., & Kanamori, H. (2022). The 2021 South Sandwich Island Mw 8.2 Earthquake: A Slow Event Sandwiched Between Regular Ruptures. *Geophysical Research Letters*, *49*(3), e2021GL097104. doi: 10.1029/2021gl097104

Kataoka, K., Urabe, A., Nishii, R., Matsumoto, T., Niiya, H., Watanabe, N., ... Miyabuchi, Y. (2024). Extensive liquefaction and building damage on the Niigata Plain due to the 1 January 2024 Noto Peninsula Earthquake: Geomorphological and geological aspects and land-use in coastal and lowland areas. Vienna, Austria: Copernicus Meetings. (Conference Name: EGU24) doi: 10.5194/egusphere-egu24-22541

Kato, A., & Nishimura, T. (2024). Foreshock sequence prior to the 2024 M7.6 Noto-Hanto earthquake, Japan. Vienna, Austria: Copernicus Meetings. (Conference

Name: EGU24) doi: 10.5194/egusphere-egu24-22522

Kennett, B. L., & Engdahl, E. R. (1991). Traveltimes for global earthquake location and phase identification. *Geophysical Journal International*, *105*(2), 429–465. doi: 10.1111/j.1365-246x.1991.tb06724.x

Kikuchi, M., & Kanamori, H. (1982). Inversion of complex body waves. *Bulletin of the Seismological Society of America*, *72*(2), 491–506. doi: 10.1785/BSSA0720020491

Koshimura, S., Adriano, B., Mizutani, A., Mas, E., Ohta, Y., Nagata, S., ... Suzuki, T. (2024). The Impact of the 2024 Noto Peninsula Earthquake Tsunami. Vienna, Austria: Copernicus Meetings. (Conference Name: EGU24) doi: 10.5194/egusphere-egu24-22523

Krischer, L., Megies, T., Barsch, R., Beyreuther, M., Lecocq, T., Caudron, C., & Wassermann, J. (2015). ObsPy: a bridge for seismology into the scientific Python ecosystem. *Computational Science & Discovery*, *8*(1), 014003. doi: 10.1088/1749-4699/8/1/014003

Lee, S.-J., Huang, B.-S., Ando, M., Chiu, H.-C., & Wang, J.-H. (2011). Evidence of large scale repeating slip during the 2011 Tohoku-Oki earthquake. *Geophysical Research Letters*, *38*(19). doi: 10.1029/2011GL049580

Lee, S.-J., Ma, K.-F., & Chen, H.-W. (2006). Three-dimensional dense strong motion waveform inversion for the rupture process of the 1999 Chi-Chi, Taiwan, earthquake. *Journal of Geophysical Research: Solid Earth*, *111*(B11). doi: 10.1029/2005JB004097

LeVeque, R. J., & George, D. L. (2008). High-Resolution Finite Volume Methods for the Shallow Water Equations With Bathymetry and Dry States. *Advanced Numerical Models for Simulating Tsunami Waves and Runup*, 43–73. doi: 10.1142/9789812790910_0002

LeVeque, R. J., George, D. L., & Berger, M. J. (2011). Tsunami modelling with adaptively refined finite volume methods. *Acta Numerica*, *20*, 211–289. doi: 10.1017/S0962492911000043

Lohman, R. B., & McGuire, J. J. (2007). Earthquake swarms driven by aseismic creep in the Salton Trough, California. *Journal of Geophysical Research: Solid Earth*, *112*(B4). doi: 10.1029/2006JB004596

Lotto, G. C., Jeppson, T. N., & Dunham, E. M. (2018). Fully Coupled Simulations of Megathrust Earthquakes and Tsunamis in the Japan Trench, Nankai Trough, and Cascadia Subduction Zone. *Pure and Applied Geophysics*, *176*(9), 4009–4041. doi: 10.1007/S00024-018-1990-Y

Madden, E. H., Ulrich, T., & Gabriel, A.-A. (2022). The State of Pore Fluid Pressure and 3-D Megathrust Earthquake Dynamics. *Journal of Geophysical Research: Solid Earth*, *127*(4), e2021JB023382. doi: 10.1029/2021JB023382

Mandli, K. T., Ahmadia, A. J., Berger, M., Calhoun, D., George, D. L., Hadjimichael, Y., ... LeVeque, R. J. (2016). Clawpack: building an open source ecosystem for solving hyperbolic PDEs. *PeerJ Computer Science*, *2*(8), e68. doi: 10.7717/PEERJ-CS.68

Masuda, H., Sugawara, D., An-Chi, Cheng, Anawat, Suppasri, Yoshinori, Shigihara, Shuichi, Kure, & Fumihiko, Imamura. (2024). *Modeling the 2024 Noto Peninsula earthquake tsunami: implications for tsunami sources in the eastern margin of the Japan Sea* (preprint). doi: 10.21203/rs.3.rs-3945364/v1

Matsushi, Y. (2024). Geomorphological consequences of the 2024 Noto Peninsula Earthquake: tectonic deformations, coseismic landslides, and their implications. Vienna, Austria: Copernicus Meetings. (Conference Name: EGU24) doi: 10.5194/egusphere-egu24-22535

Melgar, D., & Ruiz-Angulo, A. (2018). Long-Lived Tsunami Edge Waves and Shelf Resonance From the M8.2 Tehuantepec Earthquake. *Geophysical Research Letters*, *45*(22), 12,414–12,421. doi: 10.1029/2018GL080823

Minson, S. E., & Dreger, D. S. (2008). Stable inversions for complete moment ten-

sors. *Geophysical Journal International*, *174*(2), 585–592. doi: 10.1111/j.1365-246X.2008.03797.x

Miyoshi, T., Saito, T., Inazu, D., & Tanaka, S. (2015). Tsunami modeling from the seismic CMT solution considering the dispersive effect: a case of the 2013 Santa Cruz Islands tsunami. *Earth, Planets and Space*, *67*(1), 4. doi: 10.1186/s40623-014-0179-6

MLIT. (2014). *Ministry of Land, Infrastructure, Transport and Tourism (MLIT): Research Committee on Large-Scale Earthquakes in the Sea of Japan (in Japanese, translated title).* Retrieved from `https://www.mlit.go.jp/river/shinngikai_blog/daikibojishinchousa/`

Nielsen, S., & Madariaga, R. (2003). On the Self-Healing Fracture Mode. *Bulletin of the Seismological Society of America*, *93*(6), 2375–2388. doi: 10.1785/0120020090

Nielsen, S., Taddeucci, J., & Vinciguerra, S. (2010). Experimental observation of stick-slip instability fronts. *Geophysical Journal International*, *180*(2), 697–702. doi: 10.1111/j.1365-246X.2009.04444.x

Nishimura, T., Hiramatsu, Y., & Ohta, Y. (2023). Episodic transient deformation revealed by the analysis of multiple GNSS networks in the Noto Peninsula, central Japan. *Scientific Reports*, *13*(1), 8381. doi: 10.1038/s41598-023-35459-z

Oike, K., & Huzita, K. (1988). Relation between characteristics of seismic activity and neotectonics in Honshu, Japan. *Tectonophysics*, *148*(1), 115–130. doi: 10.1016/0040-1951(88)90165-5

Okada, Y. (1985). Surface deformation due to shear and tensile faults in a half-space. *Bulletin of the Seismological Society of America*, *75*(4), 1135–1154. doi: 10.1785/BSSA0750041135

Okada, Y. (1992). Internal deformation due to shear and tensile faults in a half-space. *Bulletin of the Seismological Society of America*, *82*(2), 1018–1040. doi: 10.1785/BSSA0820021018

Okada, Y., Kasahara, K., Hori, S., Obara, K., Sekiguchi, S., Fujiwara, H., & Yamamoto, A. (2004). Recent progress of seismic observation networks in Japan —Hi-net, F-net, K-NET and KiK-net—. *Earth, Planets and Space*, *56*(8), xv–xxviii. doi: 10.1186/BF03353076

Okuwaki, R., Yagi, Y., Murakami, A., & Fukahata, Y. (2024). *A Multiplex Rupture Sequence under Complex Fault Network due to Preceding Earthquake Swarms during the 2024 Mw 7.5 Noto Peninsula, Japan, Earthquake* [preprint]. (Publisher: EarthArXiv)

Olalotiti-Lawal, F., & Datta-Gupta, A. (2018). A multiobjective Markov chain Monte Carlo approach for history matching and uncertainty quantification. *Journal of Petroleum Science and Engineering*, *166*, 759–777. doi: 10.1016/j.petrol.2018.03.062

Qian, Y., Ni, S., Wei, S., Almeida, R., & Zhang, H. (2017). The effects of core-reflected waves on finite fault inversions with teleseismic body wave data. *Geophysical Journal International*, *211*(2), 936–951. doi: 10.1093/gji/ggx338

Ray, A., Alumbaugh, D. L., Hoversten, G. M., & Key, K. (2013). Robust and accelerated Bayesian inversion of marine controlled-source electromagnetic data using parallel tempering. *Geophysics*, *78*(6), E271–E280. doi: 10.1190/geo2013-0128.1

Rice, J. R. (1992). Chapter 20 Fault Stress States, Pore Pressure Distributions, and the Weakness of the San Andreas Fault. In B. Evans & T.-f. Wong (Eds.), *International Geophysics* (Vol. 51, pp. 475–503). Academic Press. doi: 10.1016/S0074-6142(08)62835-1

Romano, F., Gusman, A. R., Power, W., Piatanesi, A., Volpe, M., Scala, A., & Lorito, S. (2021). Tsunami Source of the 2021 MW 8.1 Raoul Island Earthquake From DART and Tide-Gauge Data Inversion. *Geophysical Research Letters*, *48*(17), e2021GL094449. doi: 10.1029/2021GL094449

Ross, Z. E., Cochran, E. S., Trugman, D. T., & Smith, J. D. (2020). 3D fault architecture controls the dynamism of earthquake swarms. *Science*, *368*(6497), 1357–1361. doi: 10.1126/science.abb0779

Sato, H., Ishiyama, T., Hashima, A., Kato, N., Van-Horne, A., Claringbould, J. S., ... Koshiya, S. (2020). Development of active fault model. *Annual Progress Reports of the Integrated Research Project on Seismic and Tsunami Hazards around the Sea of Japan (FY2019)*, 209–239.

Seabold, S., & Perktold, J. (2010). Statsmodels: Econometric and Statistical Modeling with Python. In (pp. 92–96). Austin, Texas. doi: 10.25080/Majora-92bf1922-011

Sepúlveda, I., Tozer, B., Haase, J. S., Liu, P. L.-F., & Grigoriu, M. (2020). Modeling Uncertainties of Bathymetry Predicted With Satellite Altimetry Data and Application to Tsunami Hazard Assessments. *Journal of Geophysical Research: Solid Earth*, *125*(9), e2020JB019735. doi: 10.1029/2020JB019735

Sibson, R. H. (1992). Implications of fault-valve behaviour for rupture nucleation and recurrence. *Tectonophysics*, *211*(1), 283–293. doi: 10.1016/0040-1951(92)90065-E

Taufiqurrahman, T., Gabriel, A.-A., Li, D., Ulrich, T., Li, B., Carena, S., ... Gallovič, F. (2023). Dynamics, interactions and delays of the 2019 Ridgecrest rupture sequence. *Nature*, *618*, 308–315. doi: 10.1038/s41586-023-05985-x

The Headquarters for Earthquake Research Promotion. (2024). *Evaluation of the 2024 Noto Peninsula Earthquake (in Japanese).* Retrieved from `https://www.jishin.go.jp/evaluation/seismicity_monthly`

Thompson, E. M., McBride, S. K., Hayes, G. P., Allstadt, K. E., Wald, L. A., Wald, D. J., ... Grant, A. R. R. (2019). USGS Near-Real-Time Products—and Their Use—for the 2018 Anchorage Earthquake. *Seismological Research Letters*, *91*(1), 94–113. doi: 10.1785/0220190207

Tsai, V. C., Nettles, M., Ekström, G., & Dziewonski, A. M. (2005). Multiple CMT source analysis of the 2004 Sumatra earthquake. *Geophysical Research Letters*, *32*(17). doi: 10.1029/2005GL023813

Ueno, H. (2002). Improvement of hypocenter determination procedures in the Japan Meteorological Agency. *QJ Seismol.*, *65*, 123–134.

Ulrich, T., Gabriel, A. A., & Madden, E. H. (2022). Stress, rigidity and sediment strength control megathrust earthquake and tsunami dynamics. *Nature Geoscience*, *15*(1), 67–73. doi: 10.1038/s41561-021-00863-5

U.S. Geological Survey. (2024). *M 7.5 - 2024 Noto Peninsula, Japan Earthquake.* Retrieved from `https://earthquake.usgs.gov/earthquakes/eventpage/us6000m0xl/executive`

Wald, D. J., Helmberger, D. V., & Hartzell, S. H. (1990). Rupture process of the 1987 Superstition Hills earthquake from the inversion of strong-motion data. *Bulletin of the Seismological Society of America*, *80*(5), 1079–1098. doi: 10.1785/BSSA0800051079

Wang, Y., Heidarzadeh, M., Satake, K., Mulia, I. E., & Yamada, M. (2020). A Tsunami Warning System Based on Offshore Bottom Pressure Gauges and Data Assimilation for Crete Island in the Eastern Mediterranean Basin. *Journal of Geophysical Research: Solid Earth*, *125*(10), e2020jb020293. doi: 10.1029/2020JB020293

Wessel, P. (2024). The Origins of the Generic Mapping Tools: From Table Tennis to Geoscience. *Perspectives of Earth and Space Scientists*, *5*(1), e2023CN000231. doi: 10.1029/2023CN000231

Wirp, A. S., Gabriel, A. A., Schmeller, M., H. Madden, E., van Zelst, I., Krenz, L., ... Rannabauer, L. (2021). 3D Linked Subduction, Dynamic Rupture, Tsunami, and Inundation Modeling: Dynamic Effects of Supershear and Tsunami Earthquakes, Hypocenter Location, and Shallow Fault Slip. *Frontiers in Earth Science*, *9*, 177. doi: 10.3389/feart.2021.626844

Xu, L., Mohanna, S., Meng, L., Ji, C., Ampuero, J.-P., Yunjun, Z., ... Liang, C. (2023). The overall-subshear and multi-segment rupture of the 2023 Mw7.8 Kahramanmaraş, Turkey earthquake in millennia supercycle. *Communications Earth & Environment*, *4*(1), 1–13. doi: 10.1038/s43247-023-01030-x

Yao, H., Gerstoft, P., Shearer, P. M., & Mecklenbräuker, C. (2011). Compressive sensing of the Tohoku-Oki Mw 9.0 earthquake: Frequency-dependent rupture modes. *Geophysical Research Letters*, *38*(20). doi: 10.1029/2011GL049223

Yoshida, K., Uchida, N., Matsumoto, Y., Orimo, M., Okada, T., Hirahara, S., ... Hino, R. (2023). Updip Fluid Flow in the Crust of the Northeastern Noto Peninsula, Japan, Triggered the 2023 Mw 6.2 Suzu Earthquake During Swarm Activity. *Geophysical Research Letters*, *50*(21), e2023GL106023. doi: 10.1029/2023GL106023

Zal, H. J., Jacobs, K., Savage, M. K., Yarce, J., Mroczek, S., Graham, K., ... Henrys, S. (2020). Temporal and spatial variations in seismic anisotropy and VP/VS ratios in a region of slow slip. *Earth and Planetary Science Letters*, *532*, 115970. doi: 10.1016/j.epsl.2019.115970

Zhu, L., & Rivera, L. A. (2002). A note on the dynamic and static displacements from a point source in multilayered media. *Geophysical Journal International*, *148*(3), 619–627. doi: 10.1046/j.1365-246X.2002.01610.x

Zhu, W., Allison, K. L., Dunham, E. M., & Yang, Y. (2020). Fault valving and pore pressure evolution in simulations of earthquake sequences and aseismic slip. *Nature Communications*, *11*(1), 4833. doi: 10.1038/s41467-020-18598-z

Supporting Information for "Rapid earthquake-tsunami modeling: The multi-event, multi-segment complexity of the 2024 M_W 7.5 Noto Peninsula Earthquake governs tsunami generation"

Fabian Kutschera[1], Zhe Jia[1], Bar Oryan[1], Jeremy Wing Ching Wong[1],

Wenyuan Fan[1], Alice-Agnes Gabriel[1,2]

[1]Institute of Geophysics and Planetary Physics, Scripps Institution of Oceanography, University of California San Diego, La Jolla, USA

[2]Institute of Geophysics, Ludwig-Maximilians-Universität München, Munich, Germany

Contents of this file

Additional Supporting Information (Files uploaded separately)

Corresponding author: F. Kutschera, Institute of Geophysics and Planetary Physics, Scripps Institution of Oceanography, University of California San Diego, La Jolla, USA. (fkutschera@ucsd.edu)

April 13, 2024, 3:36pm

Overview

We show the slip distribution of the first (USGS-T) and second (USGS-T+G) finite-fault model of the U.S. Geological Survey (2024) in Fig. S1. Next, we show the comparison of observed and synthetic seismic waveforms as used for the multiple subevent centroid moment tensor (CMT) inversion (Figs. S2-S7). Additionally, we show the uncertainties in the Bayesian 6-subevent CMT solutions obtained with the Markov Chain Monte Carlo (MCMC) inversion (Figs. S8, S9). Fig. S10 shows the vertical surface deformation of the preferred multi-CMT solution (also shown in Fig. 2) compared against aftershocks and against the fault traces from Fujii and Satake (2024) and MLIT (2014). This figure also shows the vertical displacement of the minimum and maximum offshore uplift multi-CMT solutions. Figs. S11-S13 show additional comparisons of simulated tsunami waveforms using the the USGS models, the minimum and the maximum offshore uplift multi-CMT solutions.

Tables S1, S2, and S3 provide source parameters of the preferred multi-CMT solution, information about the six subevents mapped to the corresponding fault segments, and the nodal plane standard deviations of the multi-CMT subevent solutions, respectively. Tables S4 and S5 provide insight into the arrival times of the initial tsunami crest and maximum simulated tsunami amplitudes.

Movie S1 shows a 3D view of the fault segments from the preferred multi-CMT solution together with the 30-hour aftershocks. Movie S2 shows the simulated tsunami based on the preferred multi-CMT solution. The full animations are available online.

Data Set S1. We will upload our subsampled 2000 multi-CMT solutions and all data required to reproduce our tsunami simulations to an openly available Zenodo repository.

Movie S1. 3D view of the fault segments from the preferred multi-CMT solution together with the 30-hour aftershocks.

Movie S2. Tsunami propagating based on the preferred multi-CMT solution for the three hours of simulated time.

References

Fujii, Y., & Satake, K. (2024). Slip distribution of the 2024 Noto Peninsula earthquake (MJMA 7.6) estimated from tsunami waveforms and GNSS data. *Earth, Planets and Space*, *76*(1), 44. doi: 10.1186/s40623-024-01991-z

Koshimura, S., Adriano, B., Mizutani, A., Mas, E., Ohta, Y., Nagata, S., ... Suzuki, T. (2024). The Impact of the 2024 Noto Peninsula Earthquake Tsunami. Vienna, Austria: Copernicus Meetings. (Conference Name: EGU24) doi: 10.5194/egusphere-egu24-22523

Masuda, H., Sugawara, D., An-Chi, Cheng, Anawat, Suppasri, Yoshinori, Shigihara, Shuichi, Kure, & Fumihiko, Imamura. (2024). *Modeling the 2024 Noto Peninsula earthquake tsunami: implications for tsunami sources in the eastern margin of the Japan Sea* (preprint). doi: 10.21203/rs.3.rs-3945364/v1

MLIT. (2014). *Ministry of Land, Infrastructure, Transport and Tourism (MLIT): Research Committee on Large-Scale Earthquakes in the Sea of Japan (in Japanese, translated title).* Retrieved from `https://www.mlit.go.jp/river/shinngikai_blog/daikibojishinchousa/`

U.S. Geological Survey. (2024). *M 7.5 - 2024 Noto Peninsula, Japan Earthquake.* Retrieved from https://earthquake.usgs.gov/earthquakes/eventpage/us6000m0xl/executive

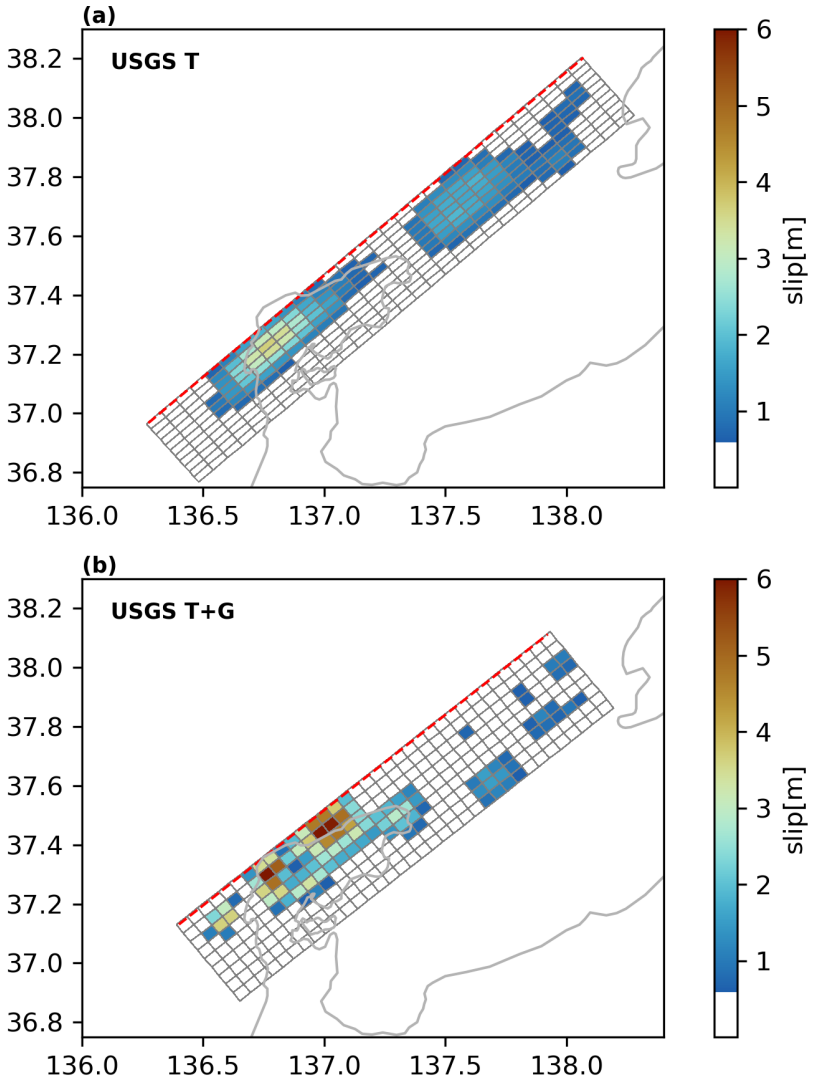

Figure S1. Slip distributions of (a) the first (USGS-T) and (b) the second (USGS-T+G) finite-fault model (U.S. Geological Survey, 2024).

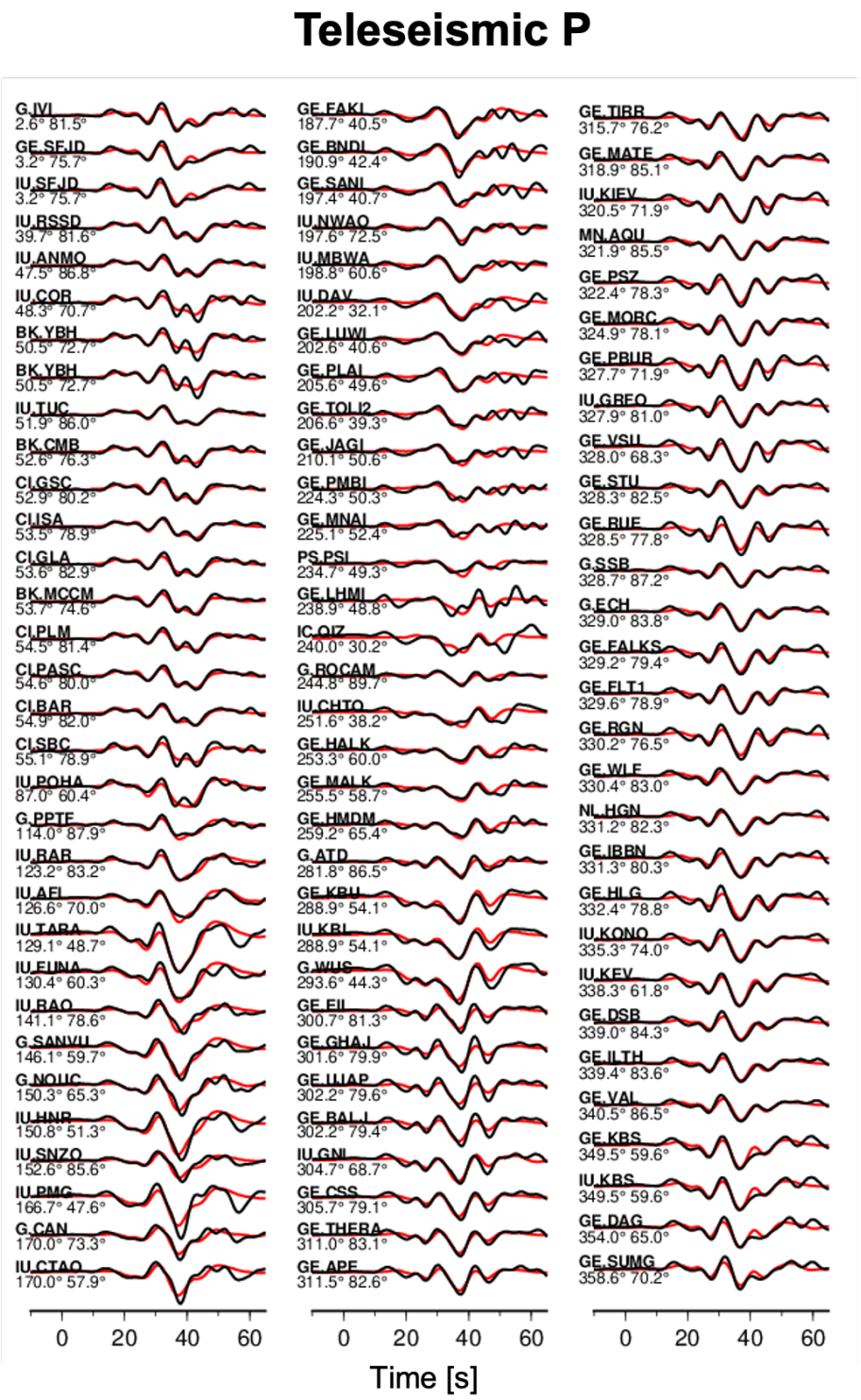

Figure S2. Observed (black) and synthetic (red) waveform fits for 93 teleseismic P waves in displacement. The numbers leading the traces are azimuths and distances.

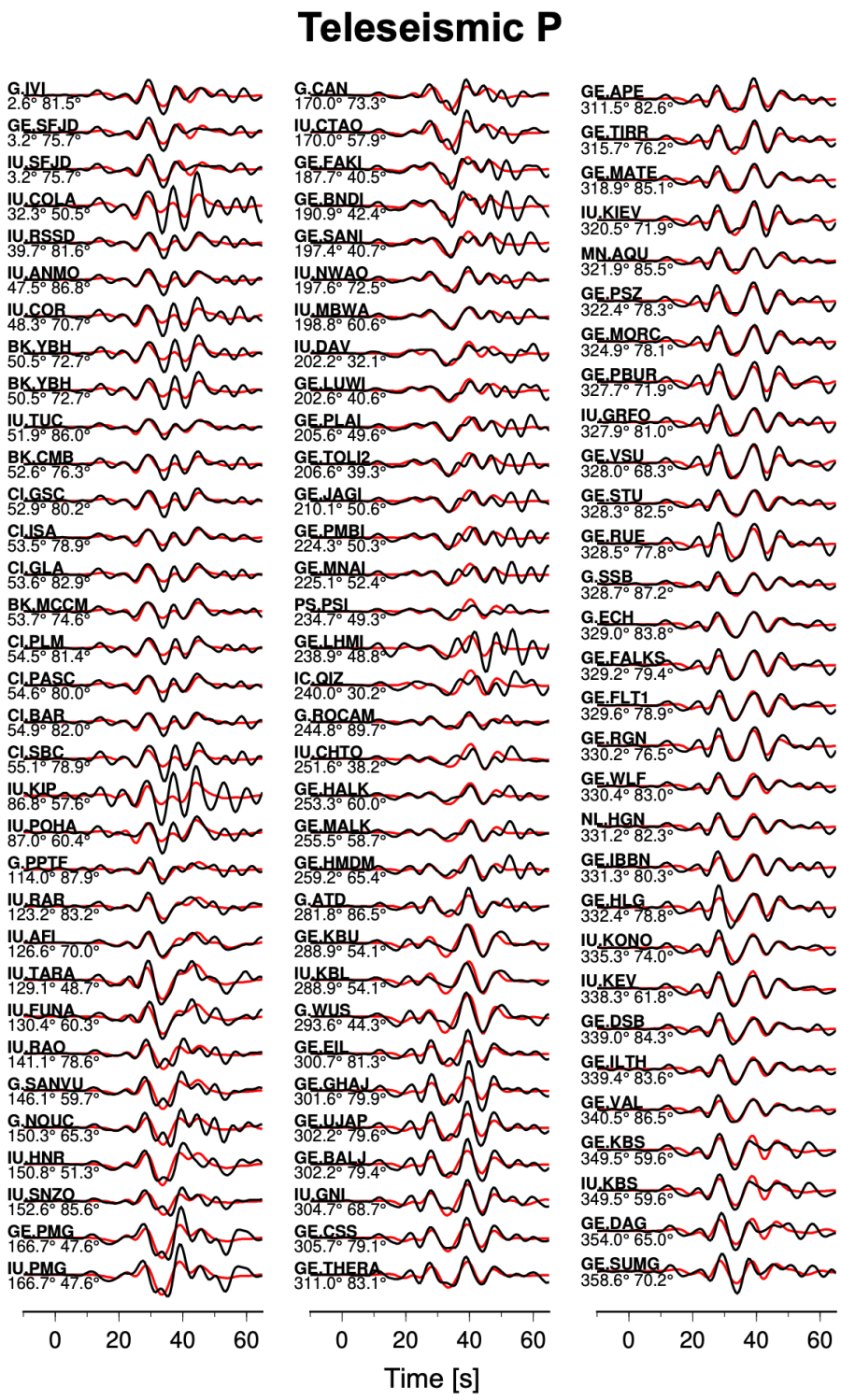

Figure S3. Observed (black) and synthetic (red) waveform fits for 93 teleseismic P waves in velocity, critical to fit the middle to high frequency content of the seismic radiation to far-fields. The numbers leading the traces are azimuths and distances.

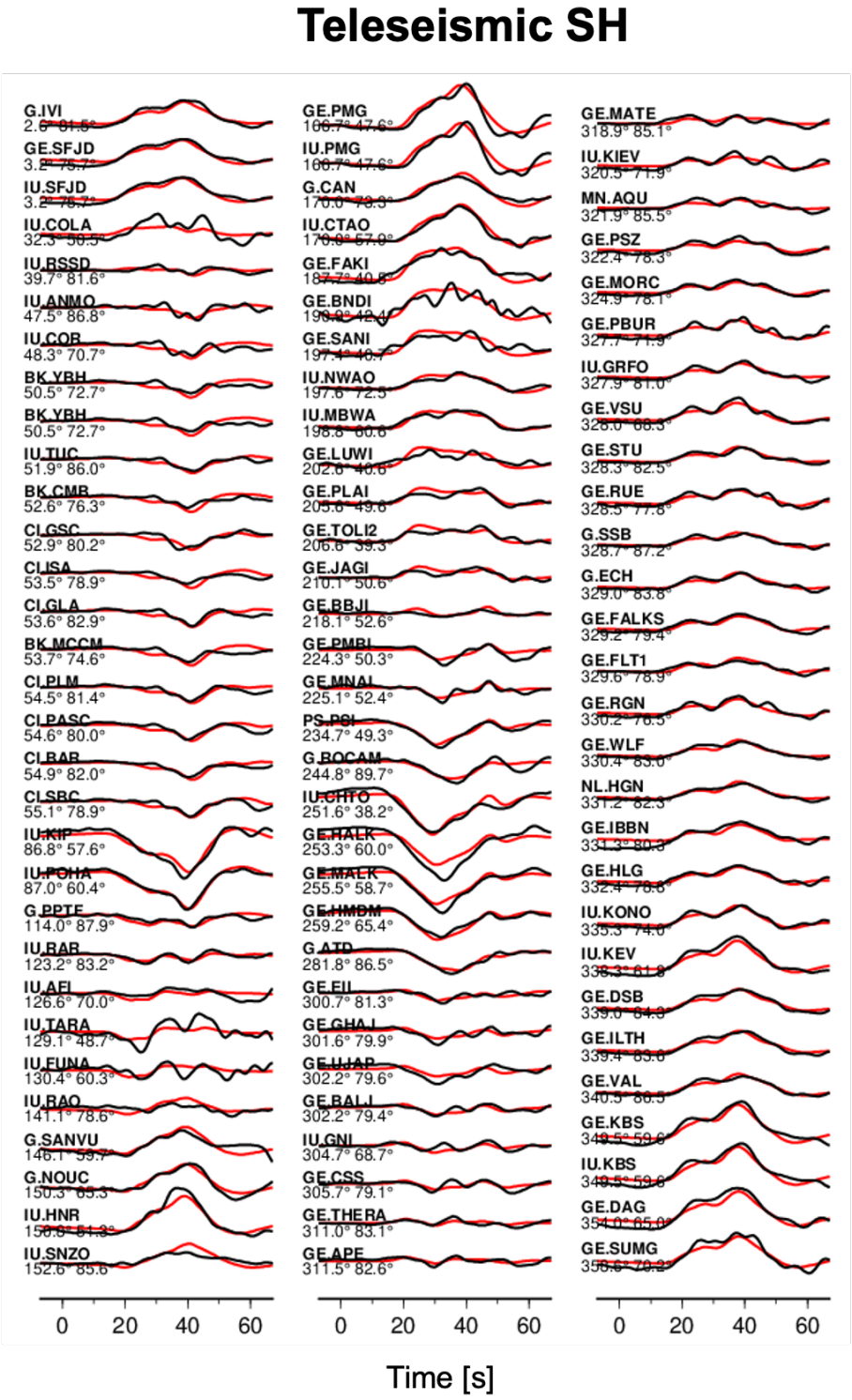

Figure S4. Observed (black) and synthetic (red) waveform fits for 93 teleseismic SH waves in displacement. The numbers leading the traces are azimuths and distances.

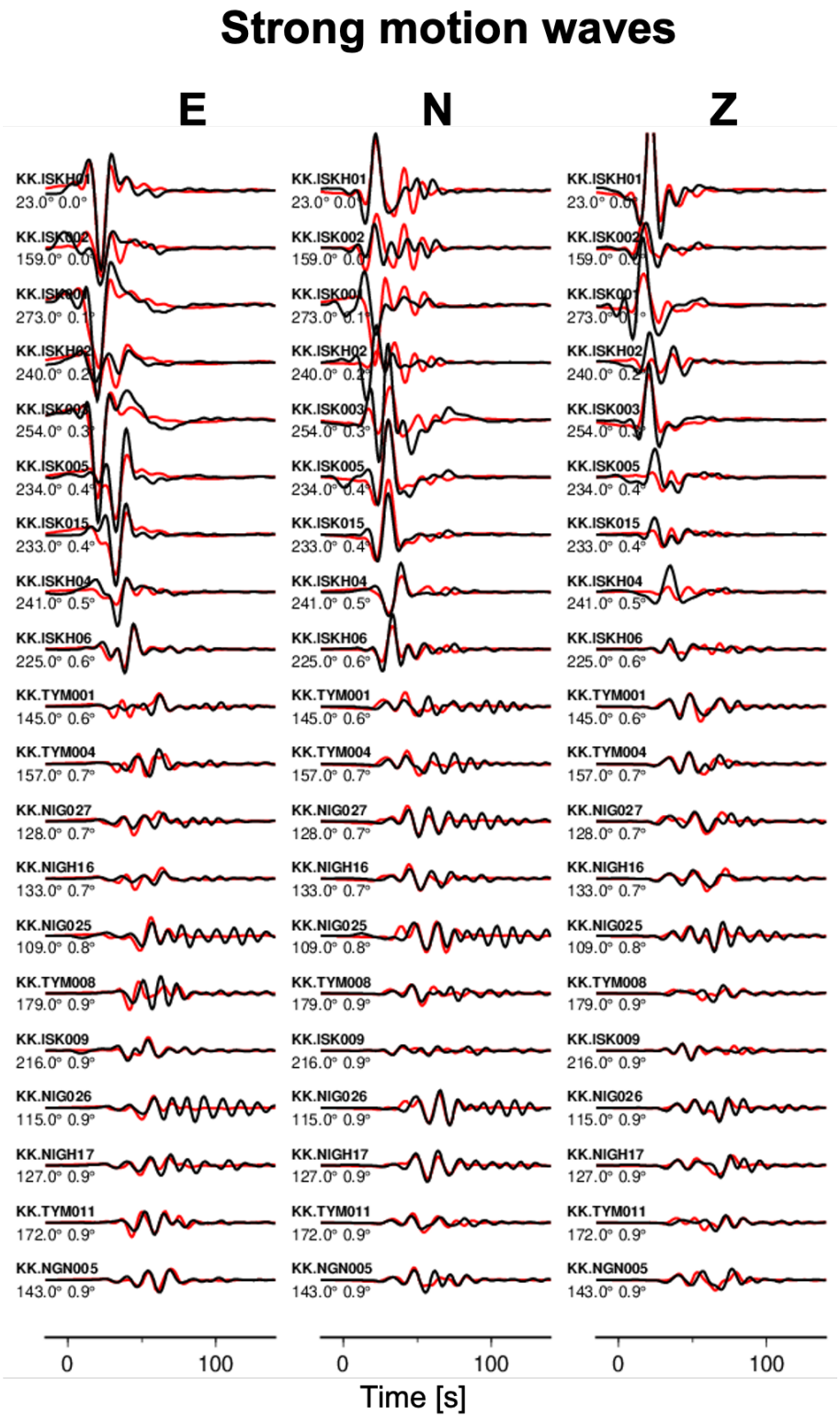

Figure S5. Observed (black) and synthetic (red) waveform fits for the first 20 (three-component) regional strong ground motion waves in displacement. The numbers leading the traces are azimuths and distances.

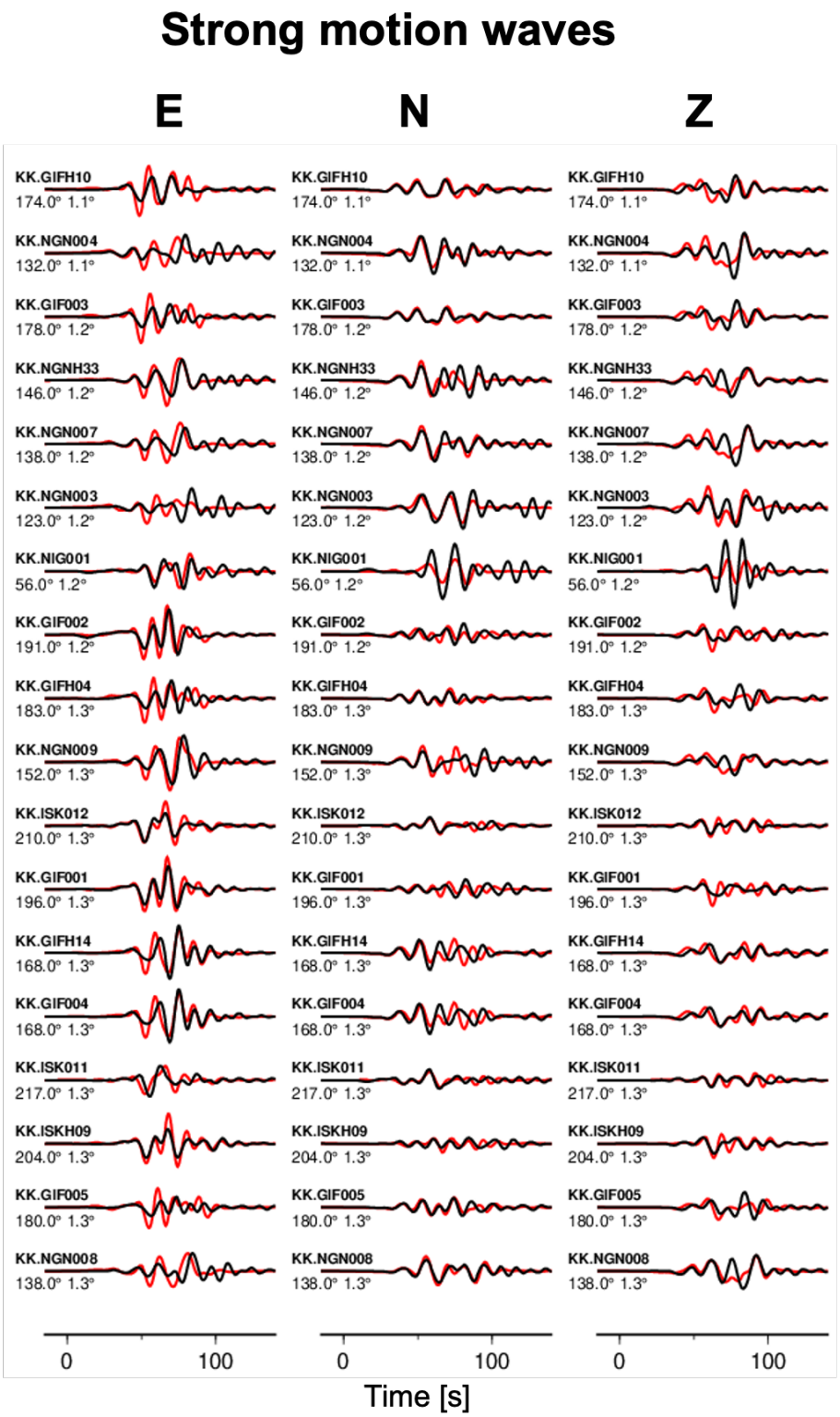

Figure S6. Observed (black) and synthetic (red) waveform fits for the second 20 (three-component) regional strong ground motion waves in displacement. The numbers leading the traces are azimuths and distances.

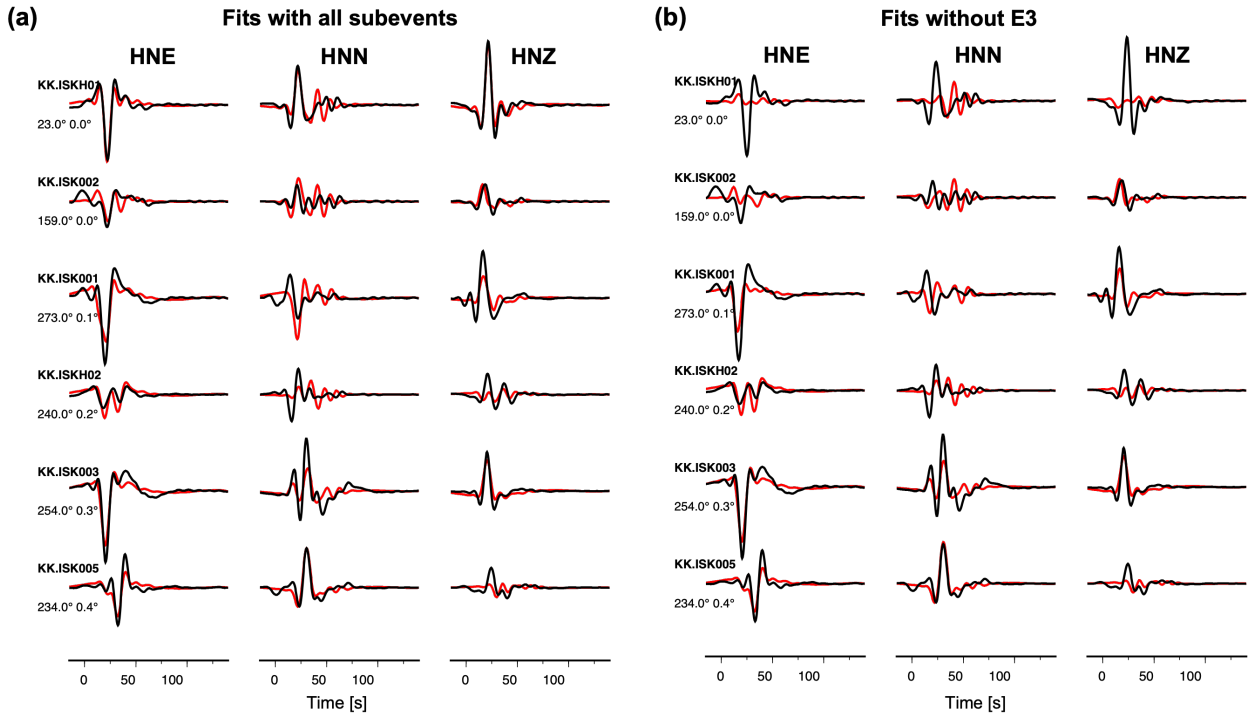

Figure S7. Comparison of strong ground motion waveforms with and without subevent E3.

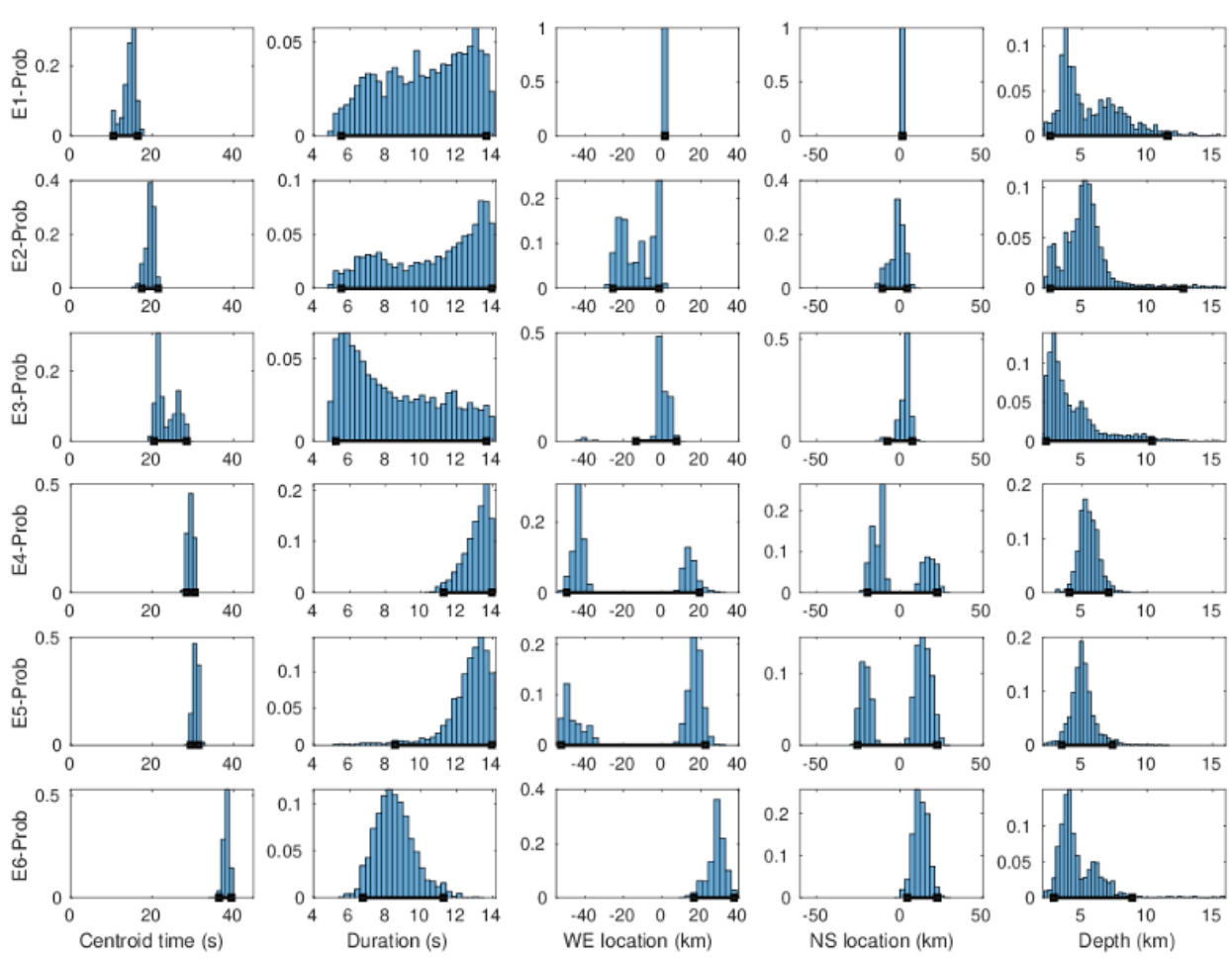

Figure S8. Centroid time, duration, West-East location, North-South location, and depth uncertainties for all six subevents (E1-E6) obtained from the multi-CMT inversion. Note that the location of the first subevent E1 is fixed at the JMA epicenter location, while its depth is allowed to vary. Black squares and lines indicate the error bars corresponding to the 95% confidential interval.

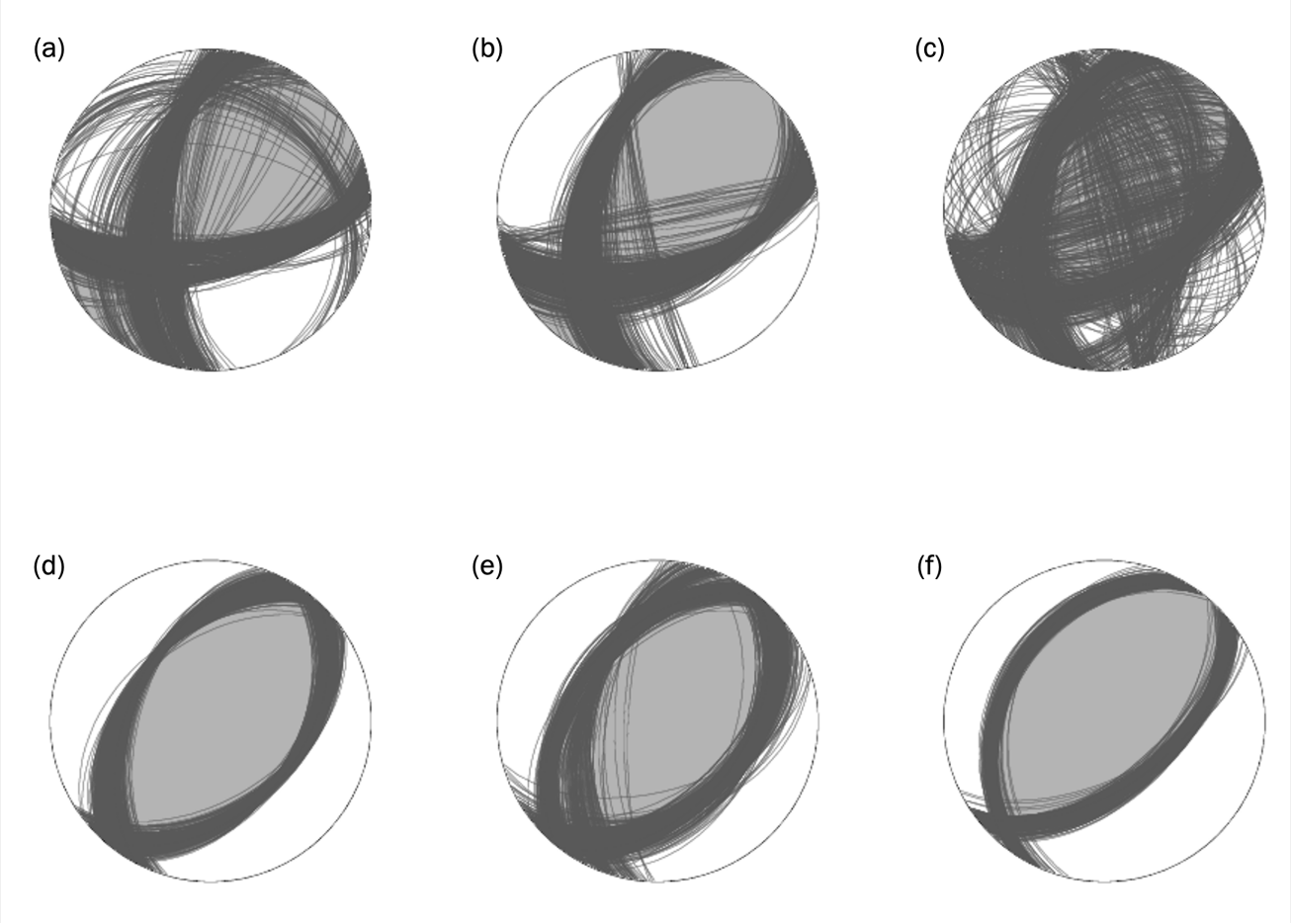

Figure S9. Fault and auxiliary plane uncertainties for all six subevents obtained from the multi-CMT inversion: (a) E1, (b) E2, (c), E3, (d) E4, (e) E5, and (f) E6.

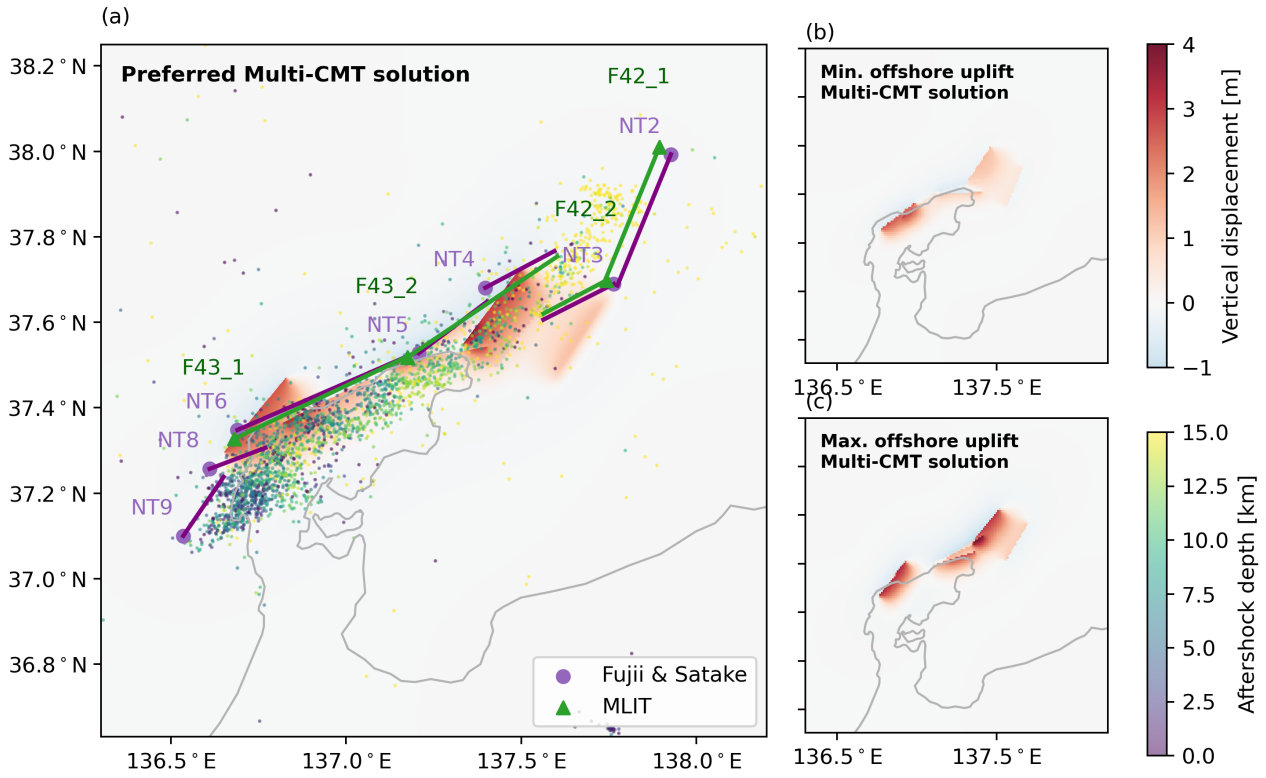

Figure S10. (a) Vertical surface deformation of the preferred multi-CMT solution (same as Fig. 2a) with the fault traces of Fujii and Satake (2024) and MLIT (2014) included. Panels (b) and (c) show the vertical displacement of the minimum and maximum offshore uplift multi-CMT solutions, respectively.

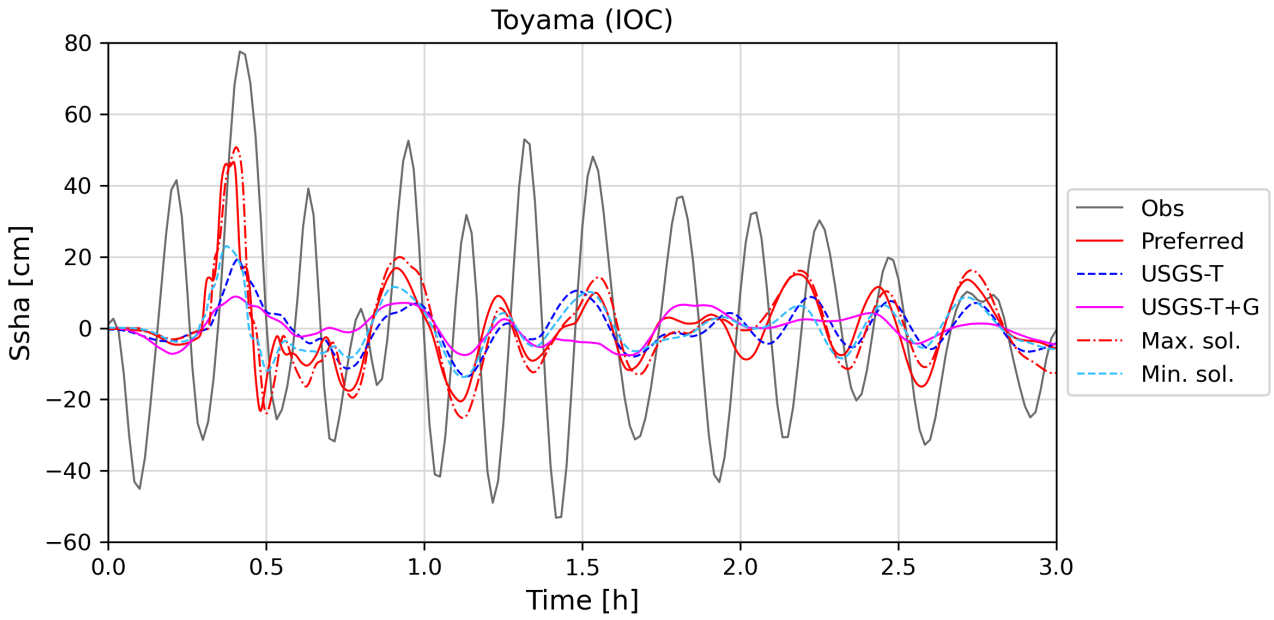

Figure S11. Comparison of observed and synthetic tsunami waveforms based on the preferred multi-CMT scenario at the tide gauge Toyama. The nearly immediate onset of the tsunami with negative polarity is likely related due to an additional contribution from a local landslide (Fujii & Satake, 2024; Koshimura et al., 2024; Masuda et al., 2024).

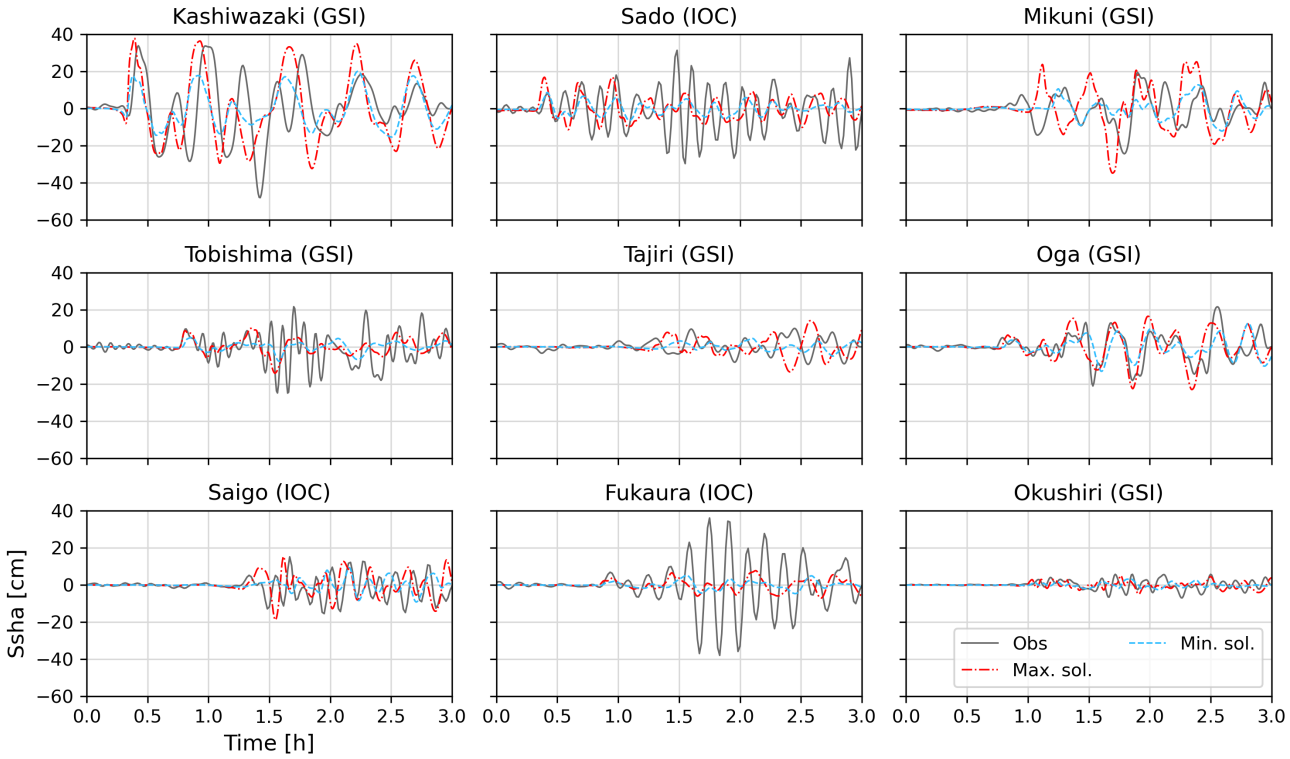

Figure S12. Comparison of observed and synthetic tsunami waveforms based on the minimum and maximum offshore uplift multi-CMT solutions at tide gauges facing the Sea of Japan, with stations sorted by their geodesic distance from the subevent E1.

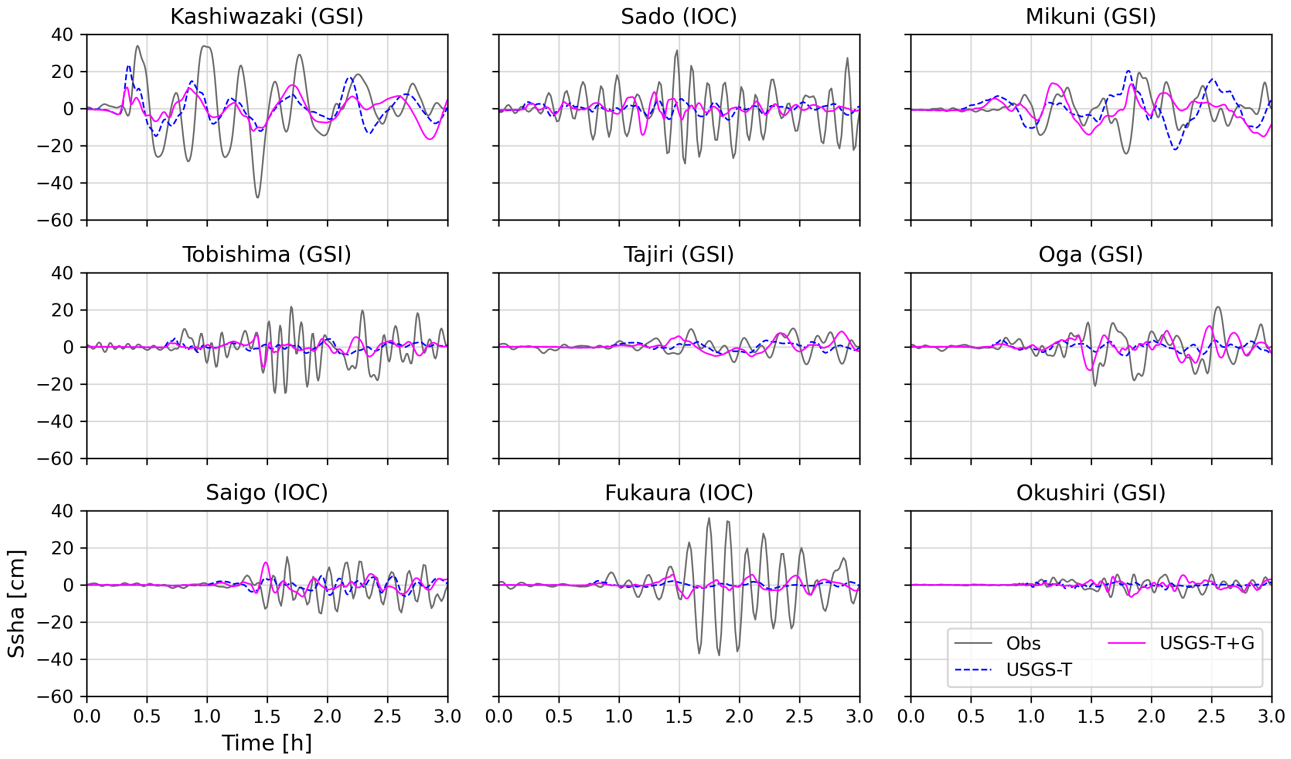

Figure S13. Comparison of observed and synthetic tsunami waveforms based on the USGS-T and USGS-T+G models at tide gauges facing the Sea of Japan, with stations sorted by their geodesic distance from the subevent E1.

Table S1. Preferred multi-CMT solution with its six subevents, E1 (top) to E6 (bottom). Latitude, longitude and depth describe the fault segment center coordinates. The units of the respective seismic moments are $1e27$ dyne-cm.

centroid time [s]	lon	lat	duration [s]	depth [km]	Mw	Mxx	Mxy	Mxz	Myy	Myz	Mzz
15.447	137.27	37.495	11.058	4.668	6.9	-0.0795	0.1924	0.0806	-0.0550	0.1135	0.1345
19.883	136.966	37.3833	13.965	5.355	7.0	-0.136	0.1916	0.1016	-0.1512	0.0648	0.2871
21.552	137.25	37.5368	6.308	2.603	6.8	-0.0535	0.0920	0.066	-0.0929	0.0474	0.1465
29.612	136.798	37.3465	13.485	6.09	7.2	-0.1699	0.3699	0.0245	-0.4663	0.0952	0.6362
30.655	137.463	37.6099	13.229	5.242	7.2	-0.2705	0.3351	-0.0073	-0.4127	-0.0043	0.6833
38.496	137.614	37.5901	8.947	6.33	6.9	-0.1428	0.1629	0.1146	-0.1555	-0.0409	0.2983

Table S2. Preferred multi-CMT solution, with the six subevents mapped to the corresponding subfaults, E1 (top) to E6 (bottom). Latitude, longitude and depth describe the fault segment center coordinates.

lon	lat	depth [km]	strike	dip	rake	length [km] (along-strike)	width [km] (along-dip)	slip [m]
137.270	37.495	4.67	81.6	56.8	145.8	25.0	11.2	2.75
136.966	37.383	5.36	64.6	51.3	119.0	25.0	13.7	2.80
137.250	37.537	2.60	62.8	51.5	124.2	25.0	6.7	3.20
136.798	37.346	6.09	41.5	42.7	100.9	25.0	18.0	4.58
137.463	37.610	5.24	38.3	45.0	89.0	25.0	14.8	5.27
137.614	37.590	6.33	214.1	36.0	74.0	25.0	15.3	2.47

Table S3. Nodal plane standard deviations of the multi-CMT subevent solutions, E1 (top) to E6 (bottom)

dip	strike	rake
9.23	46.37	67.68
8.57	28.70	34.37
14.74	88.96	101.11
1.26	4.90	6.88
2.95	8.78	13.24
2.27	6.69	5.99

Table S4. Observed and simulated arrival times of the initial tsunami crest at the tide gauge locations. The arrival time is given in minutes after origin.

Tide gauges	Observed [min]	Preferred model [min]
Kashiwazaki	25.5	24
Sado	25	24
Mikuni	56.5	55.5
Tobishima	48.5	50
Tajiri	78.5	77
Oga	47.5	51
Saigo	80	77
Fukaura	56	58
Okushiri	65	62.5

Table S5. Maximum wave amplitudes for each of the tsunami simulations as shown in Fig. 4.

	Preferred multi-CMT solution	Min. offshore uplift multi-CMT	Max. offshore uplift multi-CMT	USGS-T	USGS-T+G
Max. wave amplitude [m]	2.71	2.38	3.36	1.25	2.38